https://doi.org/10.5194/egusphere-2026-3512
Preprint. Discussion started: 17 July 2026

A comprehensive TLS-based framework for cave ice monitoring under adverse surface conditions: application at Scărișoara Ice Cave

Jozef Šupinský[1], Aurel Perşoiu[2,3,4], Michaela Nováková[1], Michal Gallay[1], Ján Kaňuk[5]

[1] Institute of Geography, Faculty of Science, Pavol Jozef Šafárik University in Košice, Košice, 04001, Slovakia
[2] Emil Racoviță Institute of Speleology, Romanian Academy, Cluj-Napoca, 400535, Romania
[3] Stable Isotope Laboratory, Ștefan cel Mare University, Suceava, 720229, Romania
[4] School of Geology, Department of Physical Geography, Aristotle University of Thessaloniki, Thessaloniki, 54124, Greece
[5] PHOTOMAP, s.r.o., Košice, 04001, Slovakia

Correspondence to: Jozef Šupinský (jozef.supinsky@upjs.sk)

Abstract. Rapid degradation of cryospheric components requires reliable quantification of volumetric change to understand the leading processes and mechanisms behind the loss of ice. However, such monitoring in cave systems, a particularly complex morphological and climatic environment, remains methodologically challenging due to irregular geometry, limited accessibility, and increasingly dynamic ice-surface conditions. This study presents a comprehensive terrestrial laser scanning (TLS) data-processing framework from noise assessment, surface reconstruction, 3D volumetric change computation and error propagation as a transferable methodology for reliable monitoring of cave ice change even under suboptimal data acquisition conditions. The framework is demonstrated at Scărișoara Ice Cave (Romania) using three annual campaigns acquired with pulse-based and phase-shift scanners under conditions ranging from optimal dry and frozen surfaces to widespread meltwater presence. Scanner-specific noise assessment on different ice surface types reveals pronounced range, intensity and incidence angle dependent errors, demanding an efficient filtering strategy that reduces point cloud dispersion. A hybrid Poisson–MeshFix reconstruction strategy effectively fills meltwater-induced data gaps, reducing modelling error by up to five times. Multiresolution modelling tests show that 5 cm resolution provides an optimal balance between volumetric precision and computational efficiency with errors under 1 % compared to finer resolution models. Comparison of conventionally applied 2.5D change detection and 3D approach reveals ~20 % volumetric discrepancy, confirming that full 3D analysis is essential in such geometrically complex settings. The results reveal a cumulative ice loss of 1521 ± 65 m^3 over three years, with heterogeneous spatial patterns controlled by cave morphology and drip-water distribution. Our data clearly shows that omitting any of the evaluated processing steps would greatly bias the volume estimates.

1 Introduction

While the loss of the cryosphere is a worldwide phenomenon (IPCC, 2019), rising temperatures and shifts in precipitation patterns bring the smallest of the cryosphere's components, like small mountain glaciers, rock glaciers, permanent snowfields and ice caves, to the brink of their extinction (Marzeion et al., 2014; Kern and Perşoiu, 2013; Perşoiu et al.,

https://doi.org/10.5194/egusphere-2026-3512
Preprint. Discussion started: 17 July 2026

2021). Apart from losing the ice itself, the paleoclimatic information they have registered is also being lost, which greatly reduces our ability to place the recent climate changes in a long-term context (Spötl et al., 2014; Colucci and Guglielmin, 2019; Jouzel, 2013; Kern and Perşoiu, 2022). Contrary to surface glaciers, ice caves have both accumulation and ablation areas in the same place, preventing compensation of ice loss by flow from higher altitudes (Perşoiu and Pazdur, 2011; Perşoiu and Lauritzen, 2018), making them more vulnerable to the impact of both short and long-term climate changes. Considering the accelerated loss of cave ice worldwide (Šupinský et al., 2019; Blatnik et al., 2022; Pfeiffer et al., 2023; Pukanská et al., 2024), high-resolution temporal and spatial monitoring is required to understand how, why, and where cave ice is melting. This task is more difficult than for surface glaciers, due to the complex interplay between cave morphology and microclimate, on one hand, and ice morphology, structure and dynamics, on the other hand. Such interactions are evident when the same dripping water that freezes in caves to form ice can act as a melting factor due to slight changes in cave air temperature, or inflow of cold air could lead to both ice accumulation (if water is available) and ice loss, due to sublimation. However, quantifying ice surface and volume changes in ice caves remains methodologically challenging.

Traditional approaches for detecting changes over extended time periods include comparison of the current state with historical (Fuhrmann, 2007) and modern photographs (Perşoiu et al., 2021), distance measurements between the ice surface and fixed reference points (Ohata et al., 1994; Rachlewicz and Szczucinski, 2004; Perşoiu and Pazdur, 2011; Pflitsch et al., 2016), drilling (May et al., 2011), radiometric dating of ice (Kern et al., 2009; Kern et al., 2018a, 2018b; Stoffel et al., 2009; Spötl et al., 2014) or total station surveys (Gašinec et al., 2012). The inability of these methods to effectively quantify volume changes repeatedly in high spatial resolution can be addressed by employing remote sensing techniques generating dense 3D point clouds. Close-range photogrammetry (CRP) performed with a digital camera provides the highest spatial resolution and precision but requires consistent light conditions and wide scene overlaps, which constrain its use in narrow corridors with complex geometry (Securo et al., 2022; Bartoš et al., 2023). Mobile laser scanning (MLS) is the most time-efficient and data-shadow-avoiding method (Zlot and Bosse, 2014; Dušeková et al., 2024), but the continuous movement results in the lowest spatial resolution and precision, limiting its application to longer intervals between successive mappings to exceed the declared measurement error. Terrestrial laser scanning (TLS), although the most time-consuming approach due to the need for multiple scan positions to minimise data shadows, is the state-of-the-art method for monitoring ice caves owing to its independence from light conditions and its high spatial resolution and precision comparable to CRP results. This approach has already been applied in several ice caves, including Eisriesenwelt (Buchroithner and Gaisecker, 2020), Dobšinská Ice Cave (Pukanská et al., 2024), Peña Castil Ice Cave (Berenguer-Sempere et al., 2014), Slovenian ice caves (Blatnik et al., 2022) and Silická ľadnica (Šupinský et al., 2019). Despite these recent TLS applications in caves, systematic and standardised TLS-based monitoring remains limited. The conducted studies primarily focus on caves under active management or rely on small representative areas, and temporally inconsistent monitoring, which restricts their applicability for long-term ice-change assessment. Consequently, the identification of the processes and mechanisms controlling ice melting and accumulation is constrained, limiting the understanding of how cave ice responds to present-day climate and weather variability. Moreover, increasingly dynamic and adverse ice-surface conditions and different ice-surface types, such

https://doi.org/10.5194/egusphere-2026-3512
Preprint. Discussion started: 17 July 2026

as semi-transparent, wet and geometrically complex ice, degrade measurement quality, while no standardised data-processing workflow has been published to ensure comparability across studies.

An additional challenge is also the interaction between laser scanner characteristics and ice surface conditions. Laser scanners operating at 1550 nm, typically used for TLS monitoring of ice caves (Šupinský et al., 2019; Buchroithner and Gaisecker, 2020; Blatnik et al., 2022; Pukanská et al., 2024), provide reduced penetration into ice compared with shorter wavelengths but remain sensitive to meltwater, partial transparency and specular reflections, resulting in elevated noise and data gaps under wet conditions (Deems et al., 2013). Laser scanning system using shorter wavelengths, such as 532 nm, penetrates deeper inside the ice, leading to erroneous measurements, while systems operating around 900 nm can partially improve spatial coverage in wet areas but are predominantly deployed on mobile platforms with inherently lower accuracy and limited effective range (Dušeková et al., 2024). These instrument-dependent differences underscore the need for explicit noise characterisation as an integral part of any ice monitoring workflow.

Addressing these limitations for long-term ice-change monitoring requires not only repeated high-resolution surveys but also a robust data-processing framework capable of handling incomplete and heterogeneous ice surface data. TLS acquisition is strongly dependent on seasonal timing, as dry and frozen surfaces provide the most stable measurement conditions, which are becoming increasingly difficult to meet under progressively milder winters, with inflow of snowmelt water and near-permanently wet ice surfaces. Monitoring must therefore account for surveys conducted under suboptimal conditions, including wet, partially melted and highly reflective surfaces introducing noise, false reflections and data gaps. In this context, the aim of this paper is to present a comprehensive and transferable TLS data-processing framework for monitoring and quantifying volumetric change of cave ice, systematically evaluating the impact of key methodological decisions on the reliability of reported ice volume estimates. The framework covers the complete chain from data acquisition through scanner-specific noise filtering, 3D surface reconstruction with gap repair, volumetric change computation and error propagation. The proposed framework is demonstrated using data from Scărișoara Ice Cave, which hosts one of the largest known perennial cave ice accumulations worldwide. The significant ice volume, the diversity of ice surface conditions encountered across three annual campaigns, and the absence of artificial ice preservation measures make Scărișoara a valuable natural site for investigating processes related to cave ice retreat as well as for evaluating the performance and transferability of the proposed workflow under active melting conditions.

2 Study area

Scărișoara Ice Cave in NW Romania (Western Carpathian Mountains) hosts one of the world's largest (>120 000 m^3) and oldest (>10 500 years) cave glaciers (Perșoiu and Onac, 2019). The cave has been intensively studied for more than 100 years, starting with the pioneering work of Emil Racoviță (Racoviţă, 1927), revealing a wide range of information on Holocene climate (Perșoiu et al., 2017) and vegetation history (Feurdean et al., 2011); biodiversity of ice-entrapped bacteria and fungi (Itcus et al., 2018; Mondini et al., 2018; Păun et al., 2019) and ice-caves specific minerals and speleothems (Žák et

https://doi.org/10.5194/egusphere-2026-3512
Preprint. Discussion started: 17 July 2026

al., 2008, 2013). Recent observations (Perşoiu et al., 2021) have shown that increasing air temperatures and extreme summer rain events have led to the rapid loss of ice in the cave, threatening the yet unexplored wealth of information the perennial ice block hosts.

The cave has a simple morphology, with a 47 m deep shaft giving access to a large room (the Great Hall), partly occupied by the underground glacier (Fig. 1). The underground ice body divides the cave into three distinct sectors, as follows: the Church, a small, circular room with the floor partly occupied by perennial ice and temporary ice stalagmites, the Little Reservation (to the north) and the Great Reservation (to the south). The Little Reservation extends from the bottom of the ~15 m vertical side of the ice block. Close to the ice cliff, the floor is formed by massive ice that gradually thins with increased distance from the cliff, ending in a large pile of breakdowns accumulation, resembling a moraine. Beyond that, the floor of the cave, consisting of limestone, rises for about 20 m, the cave ending after a ~10 m long blind passage. To the south, an inclined passage, consisting of layered ice (the extension of the ice block) in the upper 10 m and continuing with limestone breakdowns for another ~30 m leads to the lowest part of the cave, the ice-free Great Reservation.

The ice block covers ~4000 m² in the Great Hall. From there, it extends into the three side rooms and passages, where multiple near-vertical slopes and overhangs increase the total ice-covered area to more than 7000 m² (in 2D). Considering vertical ice walls, stalagmites and overhangs, the overall ice surface is ~9000 m² (in 3D). The ice block formed through the accumulation of successive ice layers (Perşoiu and Pazdur, 2011), which in turn are the result of the freezing of infiltration water during the cold season, which extends between November and March. This water usually forms a shallow lake on top of the existing ice block and subsequently freezes to add a new layer of ice every winter. Infiltration of water during the winter leads to the addition of thin layers of so-called "floor ice" on top of the initially formed "lake ice" (Perşoiu et al., 2011). Cryogenic calcite (Žák et al., 2008), soil and other surface-derived sediments (Feurdean et al., 2011) are trapped at the bottom of each layer of lake ice, resulting in the stratified structure of the ice block. In spring and summer, heat transferred by conduction through the air column in the entrance shaft and through the rock walls, as well as warm water dripping from the ceiling of the cave partly melts the ice layer formed in winter, the resulting water being drained towards either the Little or Great Reservation. The cave has a typical microclimate for ice-hosting cavities, with mean annual air temperature ranging between –3 °C in the Great Hall and gradually warming towards the most distant passages, where temperatures hover around 2.5 °C (Perşoiu et al., 2011). In the Great Hall, the air temperatures vary between 0.1 °C in summer and –14.7 °C in winter, the latter associated with large cold air avalanches that sweep down the entrance shaft, fanning out in the Great Hall, the Church and the ice walls leading to the two Reservations. These cold air inflows lead to rapid freezing of water, a drop in relative humidity and, when maintained for longer periods of time, sublimation of ice. In the two Reservations, the variability of air temperature is muted, ranging between –8 and 2 °C, the overall amplitude decreasing to less than 0.5 °C in the warmest sections of the cave.

https://doi.org/10.5194/egusphere-2026-3512
Preprint. Discussion started: 17 July 2026

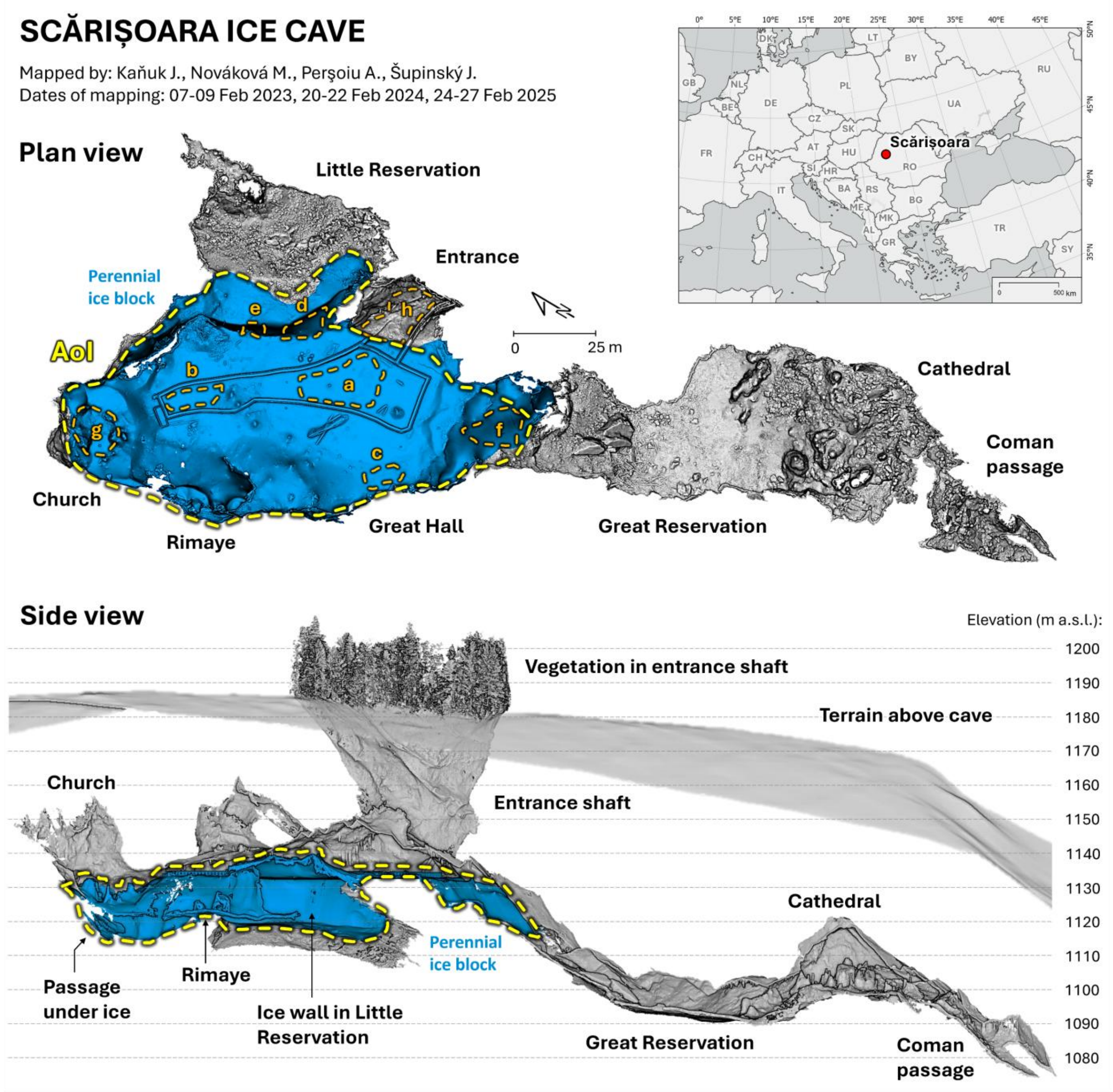

130 **Figure 1: Plan view of the Scărișoara Ice Cave derived from TLS data with highlighted area of interest (AoI) for differences of distances computation and schematically depicted evaluated areas (a–h) with different snow and ice surface conditions used for TLS accuracy assessment. Side view depicts the perennial ice block inside the AoI polygon and terrain above the cave derived from airborne laser scanning data provided by ANCPI (Agenția Națională de Cadastru și Publicitate Imobiliară).**

https://doi.org/10.5194/egusphere-2026-3512
Preprint. Discussion started: 17 July 2026

3 Methodology

Reliable TLS-based monitoring of cave ice requires careful consideration of environmental conditions and parameters of the employed device. Detectable interannual change must exceed declared measurement error, while surface state strongly affects data quality and completeness. Increasingly variable winter conditions and frequent temperature fluctuations around 0 °C promote melting and refreezing processes, leading to higher positional inaccuracy and systematic data gaps in TLS point clouds. To ensure more stable surface conditions, surveys are preferably conducted during sustained sub-zero temperatures prior to renewed ice speleothem growth. Therefore, for the established monitoring in Scărișoara Ice Cave, interannual mapping conducted once per winter, when the lowest temperatures are expected, was adopted starting February 2023.

3.1 TLS equipment and acquisition parameters

TLS data were acquired using two terrestrial laser scanners operating at a wavelength of 1550 nm, which is commonly used for snow and ice measurements due to reduced laser penetration while providing reliable measurements up to ~150 m (Deems et al., 2013; Gabbud et al., 2015). The main laser scanner was a time-of-flight RIEGL VZ-1000, acquiring up to 122 000 points per second, with a declared accuracy of 3.1 mm at 100 m based on the last calibration protocol, and a minimum scanning range of 2.5 m (RIEGL, 2015). For all scan positions collected within the cave, identical settings were applied: a pulse repetition rate of 300 kHz and an angular step of 0.04°, capturing a full 360° horizontal panorama with 100° vertical field of view, resulting in overall 20 million points per position. The phase-shift FARO Focus 3D X130 was used as a supplementary laser scanner in narrow passages and areas prone to shadowing. This more compact laser scanner measures up to 976 000 points per second, with declared accuracy of 2 mm at 10 m and a minimum scanning range of 0.6 m (FARO, 2016). Depending on the dimensions of the scanned area, acquisition settings ranged from 1/8 to 1/4 of the full scan resolution. The higher resolution of 1/4 was applied for the ice block and its surroundings, corresponding to an angular step of 0.035°, comparable to the RIEGL settings. In contrast, the FARO laser scanner offers a wider 150° vertical field of view while maintaining a full 360° horizontal panorama. Overall, from 1 to 40 million points per position were recorded, depending on scene size and applied settings.

3.2 Annual field campaigns

Due to the significant extent of the area of interest (AoI) delineated around the perennial ice block, data acquisition requires at least two days of mapping every year, involving the placement of ~200 scan positions. These were spaced up to 10 m apart to ensure the best possible coverage of the surveyed surface, with a higher density of positions used in areas prone to shadowing. TLS mapping in February 2023 was performed under stable sub-freezing temperatures, with almost all inflowing water being frozen at the time of scanning. Only small areas of partially melted floor ice were present within the area enclosed by the wooden tourist path in the Great Hall, and a few semi-transparent ice stalagmites were observed in the Church. Data were collected with both laser scanners on and around the ice block. The entrance shaft was scanned along the

https://doi.org/10.5194/egusphere-2026-3512
Preprint. Discussion started: 17 July 2026

stairs up to the entrance with the RIEGL laser scanner. Remote ice-free parts of the Great Reservation and the narrow passages around and below the ice block were scanned with the FARO laser scanner. To speed up laser scanning in ice-free parts of the cave, we used lower resolutions: 1/5 (0.044°; ~26 million points per position) in the Cathedral, and 1/8 (0.07°; ~10 million points per position) in narrow passages. In subsequent years, scan-position distribution principles and acquisition parameters were kept consistent to maintain interannual comparability, with modifications applied only to compensate for surface-state variability. The entrance shaft and previously surveyed ice-free cave parts were excluded from later campaigns, as they are outside the AoI for ice change monitoring.

Given the mild winter conditions in 2024, problematic acquisition conditions for TLS were anticipated. From 2024 onwards, the TLS monitoring was therefore supplemented with a tachymetric total station survey (TSS) using the robotic total station TOPCON GT, not only to collect tie points for co-registration but also to provide independent reference measurements for laser-scanning evaluation and, if needed, to compensate for reduced data density. The most favourable conditions for TLS mapping were observed in 2025, with constant sub-zero temperatures, most ice surfaces being covered by cryogenic calcite (as white powder) resulting from rapid freezing of drip-water, as well as sporadic occurrence of newly grown seasonal ice formations. The following processing workflow consisted of scan registration, data filtering, co-registration, surface modelling (including surface reconstruction and artefacts repair), and volumetric change computation (Fig. 2).

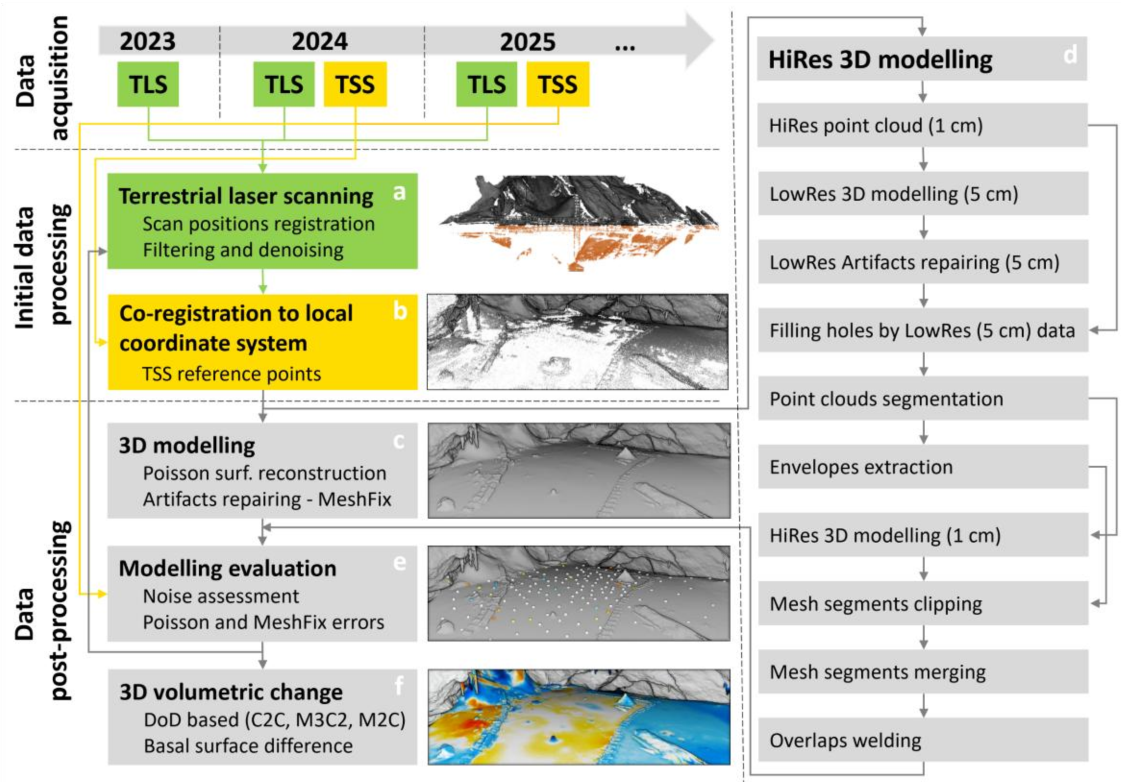

Figure 2: Processing workflow for ice accumulations monitoring using terrestrial laser scanning (TLS) and total station survey (TSS) with detailed subprocess steps for high-resolution 3D modelling (below 5 cm) for Scărișoara Ice Cave.

https://doi.org/10.5194/egusphere-2026-3512
Preprint. Discussion started: 17 July 2026

3.3 Point-cloud processing and co-registration

Initial registration of individual scan positions (Fig. 2a) from the RIEGL and FARO laser scanners was performed in RiSCAN PRO and FARO SCENE software, respectively. Quality control included exclusion of incomplete scans and scans affected by tripod instability. A deviation threshold of 10 was applied to RIEGL data to remove stray points between objects and low-quality reflections with a distorted shape of the laser footprint. Preliminary denoising of the FARO data was performed using the built-in edge artifact filter and the stray point filter with a grid size of 3 pixels, distance threshold of 1 cm, and allocation threshold of 40 %. To characterise major noise behaviour under varying ice surface conditions, a dedicated noise assessment was conducted for each scanner, providing the basis for subsequent point cloud filtering (Sect. 4.2). False reflections under ice surfaces and non-target features in the point cloud (visitors, wooden tourist path, equipment) were removed manually. Scan positions acquired with the FARO laser scanner were then imported into the RiSCAN PRO project and co-registered to the reference RIEGL scan positions for the given year. Laser scans from the same scanner and campaign were merged into a single point cloud and subsampled to a 1 cm spacing. Distance differences between the FARO and reference RIEGL point clouds were then computed using the Cloud-to-Cloud (C2C) approach in CloudCompare (Girardeau-Montaut, 2016). The final combined point cloud for each year of mapping consisted of a processed RIEGL dataset and extracted points from the FARO dataset that were located more than 2 cm from reference RIEGL data to fill unmapped areas. Co-registration of point clouds between individual years (Fig. 2b) was performed in CloudCompare using automatic ICP with the sC2C (selective Cloud-to-Cloud) approach, with the stable cave ceiling serving as the reference surface (Šupinský et al., 2019). The resulting point clouds were placed in the local coordinate system defined by the TSS, using 2025 TLS mapping by RIEGL as a reference for all co-registrations.

3.4 3D modelling

In the performed monitoring, we propose a combined approach for 3D modelling (Fig. 2c) using Poisson surface reconstruction (Kazhdan and Hoppe, 2013) with subsequent triangulation-based gap filling using the MeshFix algorithm (Attene, 2010). Poisson surface reconstruction was performed at modelling resolutions ranging from 1 to 50 cm to evaluate the sensitivity of modelling accuracy and to determine an optimal balance between spatial resolution, computational cost, and acquired volumetric precision.

The modelling parameters of Poisson surface reconstruction were uniformly set for each resolution with one point per node, a point weight of 0.8, and a Neumann boundary type, which produced satisfactory results for the 2023 and 2025 datasets. Because of the low density of point cloud data on the ice surface in 2024 (Fig. 3a), Poisson surface reconstruction produced numerous exaggerated surfaces in areas of data gaps on the flat ice surface and in the icefall area toward the Great Reservation (Fig. 3b), as the method is highly dependent on input points density and local curvature. To improve modelling artefacts in data gaps areas, the derived 3D model was clipped based on the density parameter (Fig. 3c) and resulting gaps filled using the MeshFix algorithm (Attene, 2010). The density threshold value was selected based on histogram distribution

https://doi.org/10.5194/egusphere-2026-3512
Preprint. Discussion started: 17 July 2026

(typically 3 points below the maximum) and visually checked if the resulting 3D model faces do not cross the actual ice surface in known flat areas. Before the MeshFix application, connecting isolated surfaces to the main segment was performed to prevent their removal during the filling procedure. Resulting 3D mesh models (Fig. 3d) with filled gaps successfully removed most exaggerated surfaces produced by Poisson surface reconstruction and were evaluated against reference TSS control points.

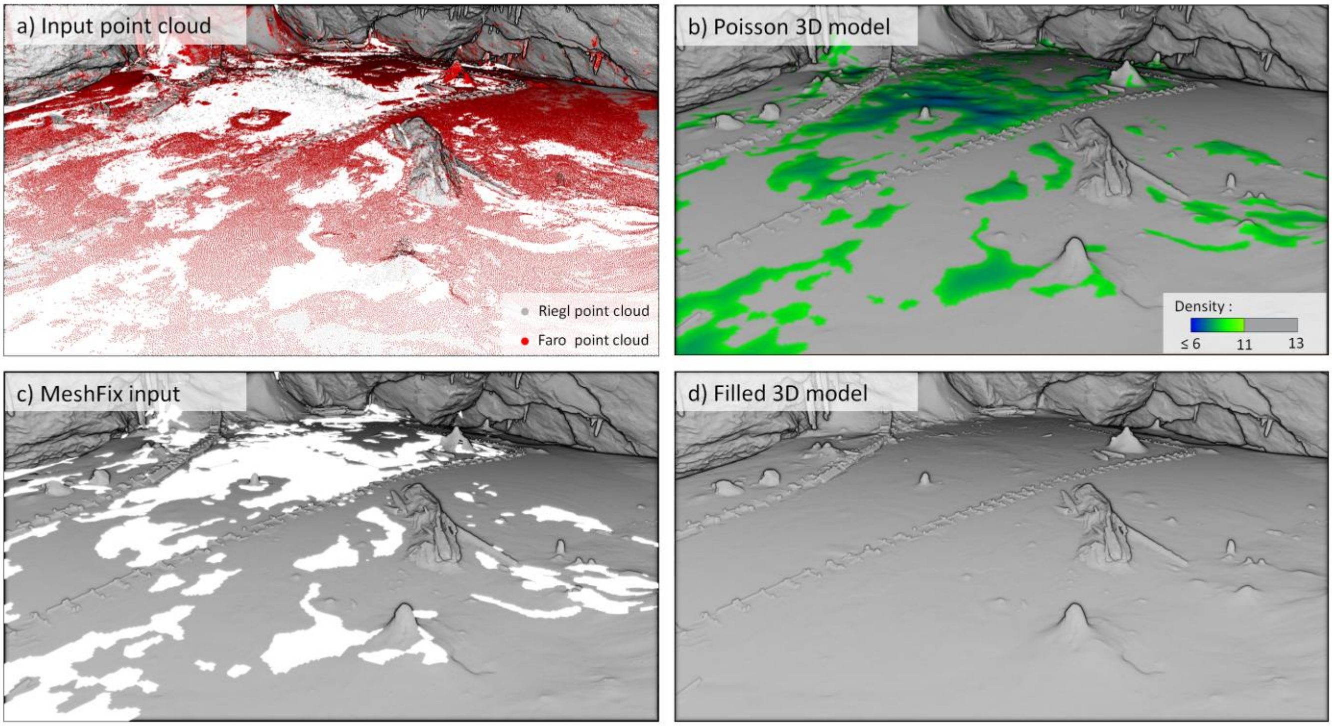

Figure 3: 3D modelling and repair of the dataset most affected by data gaps in 2024: a) Input point cloud; b) 3D mesh model generated by Poisson surface reconstruction; c) Removed low-reliability faces using density parameter; d) Resulting filled mesh model.

For modelling resolutions between 5 and 50 cm (Fig. 2d), Poisson surface reconstruction followed by MeshFix processing was performed as a single segment (Fig. 2c). In cases of high-resolution modelling at resolutions below 5 cm (Fig. 2d), the large dataset size required segmentation of the cave into multiple sections. The applied multiscale approach preserved spatial relationships, particularly in areas where complex gaps extended across multiple segments. Firstly, modelling and repairing artefacts in 5 cm for the entire cave was performed, then distances were computed for the input point cloud in higher resolution and points within distances above 5 cm were extracted to fill data gaps areas within the input point cloud. Subsequently, the cave was segmented into ~40 m sections with 1 m overlaps in each direction, resulting in 16 segments for 1 cm resolution modelling. To remove extrapolated faces from modelled surfaces along segment edges, plan-view boundary envelopes for clipping were derived, and extracted 3D mesh model segments were merged. The overlapping vertices were welded to prevent duplicate volume computation on coincident faces.

https://doi.org/10.5194/egusphere-2026-3512
Preprint. Discussion started: 17 July 2026

3.5 Accuracy assessment and volumetric change quantification

To assess TLS point clouds' accuracy and noise levels, small homogeneous areas representing different surface properties were identified (Fig. 1; Fig. 7 a–h) and compared with TSS measurements and derived mesh models. Local triangulated surfaces derived from TSS control points represented the true physical ice surface, and orthogonal distances of surrounding TLS points to these reference meshes were computed to evaluate absolute accuracy and point dispersion. The generated Poisson mesh model in 1 cm resolution was used as an internal reference to quantify residual noise by computing distances between the input TLS points and the derived TLS mesh model (Fig. 2e). Residuals obtained from both TSS and TLS-based comparisons were quantified by their standard deviations to evaluate the noise occurrence within the TLS point clouds (Table 2).

Computing differences of distances (DoD) to quantify local ice surface changes and associated volumetric change (Fig. 2f) is determined by the proportion of near-vertical and overhanging areas at the monitored site. To evaluate only ice surfaces without incorporating wider areas of the cave and thereby increasing processing error, we classified the cave into floor and ceiling using the Cloth Simulation filter (Zhang et al., 2016) and clipped floor points to the AoI extent. Interannual DoD were computed in CloudCompare using Cloud-to-Cloud (C2C) and Mesh-to-Cloud (M2C) approaches, both using the nearest distance metrics, as well as M3C2 (Lague et al., 2013), computing distances in the local normal direction. The resulting 3D volume change ΔV was calculated as the sum of face area (A_{Fi}) multiplied by corresponding per-face DoD (d_{Fi}) over all mesh faces as follows Eq. (1).

$$\Delta V = \sum_{i=1}^{n} A_{Fi} \times d_{Fi}, \quad (1)$$

The total DoD processing error E_{Total} Eq. (2) was determined as the root-sum-of-squares (RSS) of the standard deviations of the measurement device error (Dev), internal registration error (I-reg), co-registration error (Co-reg), and 3D modelling error (Model). As TSS measurements were not conducted in 2023, the 3D modelling error component derived from TSS observations was adopted from the 2025 survey, which exhibited comparable mapping conditions.

$$E_{Total} = \sqrt{\sigma_{Dev}^2 + \sigma_{I-reg}^2 + \sigma_{Co-reg}^2 + \sigma_{Model}^2}, \quad (2)$$

Volumetric error E_V was computed Eq. (3) by scaling total processing error (E_{Total}) to the evaluated area of the DoD processing AoI, representing the potential uncertainty in volumetric computations introduced by the applied devices and processing workflow.

$$E_V = E_{Total} \times A_{AoI}, \quad (3)$$

2.5D volume change was computed in CloudCompare using the Compute 2.5D Volume tool by comparing datasets between years, with a grid step size corresponding to the given model resolution and maximum height in the Z direction. Additionally, an independent volumetric change estimate was computed from enclosed manifold 3D mesh models with an identical basal surface (Šašak et al., 2024) to verify that the DoD-derived volume change was not affected by methodological

https://doi.org/10.5194/egusphere-2026-3512
Preprint. Discussion started: 17 July 2026

bias. To construct these closed 3D models, a flat horizontal basal plane was established at a depth of 20 m below the lowest point of the AoI. This ensured that the model boundary would not be breached even under a hypothetical scenario of complete melting of all cave ice.

To share and visualise the resulting DoD 3D mesh models, a web-based interface built on the Three.js JavaScript library (Cabello, 2010) was developed, using the Nexus mesh format (Cignoni et al., 2005) for efficient model rendering. This platform allows users to interactively examine and compare spatial changes across the cave.

4 Results

The results are structured to link acquisition conditions to change-detection performance. Registration errors and point-cloud coverage achieved for each campaign are first reported (Table 1; Figs. 4–5), followed by analysis of surface-dependent noise (Figs. 6–8). Modelling-resolution effects are then assessed, and improvements in surface representation obtained through mesh repair in the year affected by meltwater-induced data gaps are demonstrated (Table 2; Fig. 9). Based on these evaluations, the most robust DoD estimates of interannual ice-surface and volumetric change within the AoI are presented (Figs. 10–11).

4.1 Acquired TLS data and processing errors

TLS acquisition resulted in large multi-billion point datasets for each campaign (Table 1), with raw point counts ranging from ~4.7 billion (2024) to ~7.4 billion (2025). After range filtering, noise removal, and subsampling to 1 cm spacing, 2–3 % of the original points were retained for DoD processing within the AoI (Table 1).

TLS campaign in 2023 included scanning of ice-free parts and the entrance shaft, when a total of 243 scan positions were acquired (62 RIEGL, 181 FARO). After quality control, 235 scans were retained, containing ~5.2 billion raw points. For the following years, areas outside the AoI were omitted from the survey and scan positions were gradually reorganised and densified on and around the ice block to optimise coverage of the monitored area (Fig. 5). In 2024, within 207 positions (79 RIEGL, 128 FARO) ~4.7 billion points were recorded. Nine scans affected by minor positional shifts during acquisition were excluded in the quality control process. The collection of control points using TSS was performed on the last day of mapping in the Great Hall, where the most extensive ice melting was observed. Five tie points were measured to co-register the TSS and TLS datasets, along with 405 control points used to evaluate scanning and modelling accuracy. In 2025, a total of 242 scan positions (91 RIEGL, 151 FARO) were successfully acquired, producing ~7.4 billion raw points. The total station survey resulted in the collection of five tie points together with 146 control points in the Great Hall area.

Intra-annual registration error was consistently low, with standard deviations below 4 mm for the combined datasets across all years (Table 1). The 2023 dataset exhibited slightly higher FARO registration error (3.8 mm) due to larger scan-position spacing in ice-free areas. Considering only the AoI, the registration error was 3.6 mm.

https://doi.org/10.5194/egusphere-2026-3512
Preprint. Discussion started: 17 July 2026

The lowest overall registration errors (2.7 mm for RIEGL and 3.4 mm for FARO) were achieved in 2025 under stable frozen conditions. In contrast, the 2024 dataset showed slightly higher registration uncertainty (3.2 mm for RIEGL and 3.5 mm for FARO), which is attributed to meltwater-affected surfaces causing false reflections and reducing the number of usable planar registration objects on the ice.

Interannual co-registration, constrained to stable ceiling surfaces, yielded residual standard deviations of 3.7 mm for 2023 and 3.5 mm for 2024 relative to the 2025 reference dataset (Fig. 4). White and grey areas in Fig. 4 indicate near-zero differences between interannual datasets on the cave ceiling and stable ice-free floor areas, while orange and red areas point to areas of ice surface difference or different coverage of collected datasets (e.g., the entrance shaft or chimneys). Integration of TLS and TSS data resulted in processing errors of 4.4 mm in 2024 and 3.2 mm in 2025.

Table 1: Summary statistics of processed point clouds.

2023	**RIEGL**	**FARO**	**Co-Registered**
Used scan positions / Total	61 / 62	174 / 181	235 / 243
Processing error StdDev (mm)	2.7	3.8	3.3
Initial raw point cloud	1 104 297 337 (100 %)	4 092 367 587 (100 %)	5 196 664 924 (100 %)
Filtered point cloud	784 818 255 (71 %)	3 631 098 038 (89 %)	4 415 916 293 (85 %)
Subsampled point cloud to 1 cm	143 472 711 (12.9 %)	221 367 209 (5.4 %)	364 839 920 (7.0 %)
Clipped and comb. p. cloud for DoD	113 746 377 (10.3 %)	32 319 752 (0.8 %)	146 066 129 (2.8 %)

2024	**RIEGL**	**FARO**	**Co-Registered**
Used scan positions / Total	74 / 79	124 / 128	198 / 207
Processing error StdDev (mm)	3.2	3.5	3.4
Initial raw point cloud	1 146 715 251 (100 %)	3 572 489 112 (100 %)	4 719 204 363 (100 %)
Filtered point cloud	846 905 502 (74 %)	2 646 917 535 (74 %)	3 493 823 037 (74 %)
Subsampled point cloud to 1 cm	120 170 076 (10.4 %)	161 265 780 (4.5 %)	281 435 856 (5.9 %)
Clipped and comb. p. cloud for DoD	97 268 780 (8.4 %)	49 754 861 (1.4 %)	147 023 641 (3.1 %)

2025	**RIEGL**	**FARO**	**Co-Registered**
Used scan positions / Total	91 / 91	151 / 151	242 / 242
Processing error StdDev (mm)	2.7	3.4	3.2
Initial raw point cloud	1 811 034 777 (100 %)	5 582 959 241 (100 %)	7 393 994 018 (100 %)
Filtered point cloud	1 289 451 869 (71 %)	4 474 927 762 (80 %)	5 764 379 631 (78 %)
Subsampled point cloud to 1 cm	154 148 319 (8.5 %)	174 362 536 (3.1 %)	328 510 855 (4.4 %)
Clipped and comb. p. cloud for DoD	128 405 726 (7.1 %)	29 001 270 (0.5 %)	157 406 996 (2.1 %)

https://doi.org/10.5194/egusphere-2026-3512
Preprint. Discussion started: 17 July 2026

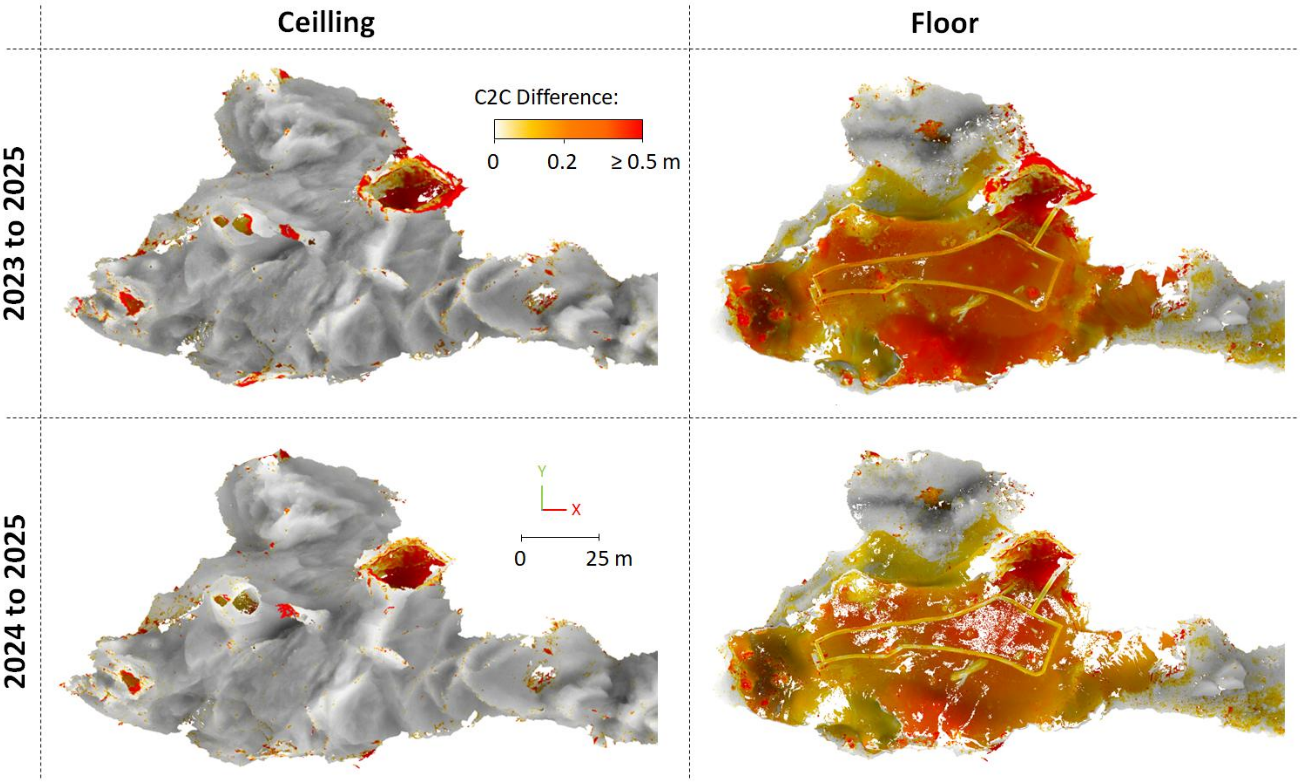

Figure 4: Results of co-registration of the combined datasets.

Surface coverage varied between campaigns, with near-complete coverage of the ice block in 2023 and 2025, and reduced coverage (~70 %) in 2024 due to meltwater-induced data gaps. The average density of the fully merged datasets subsampled to 1 cm was ~14 000 points m^{-2} for 2023 and 2025, and ~12 500 points m^{-2} for 2024. Considering only floor points within the ice block (Fig. 5), the average point density for the RIEGL dataset ranges from ~2700 points m^{-2} in 2024 to ~5000 points m^{-2} in 2025, while the FARO dataset ranges from ~5100 points m^{-2} to ~6700 points m^{-2} over the same period. The combined point cloud reaches ~6000 points m^{-2} in 2023 and 2025 and decreases to ~5000 points m^{-2} in 2024, while exhibiting improved spatial homogeneity of point distribution.

A denser placement of FARO scan positions improved the sampling of wet ice surfaces, and FARO points represented 22.1 % (2023) and 33.8 % (2024) of the combined point cloud, filling gaps in the RIEGL datasets (Fig. 5). In contrast, the denser RIEGL scan-position distribution in 2025 reduced the relative contribution of FARO data to 18.4 % of the combined point cloud, with most FARO points originating from the Rimaye, passage beneath the ice block and the moraine in the Little Reservation (Fig. 1), which were scanned exclusively using the FARO system.

https://doi.org/10.5194/egusphere-2026-3512
Preprint. Discussion started: 17 July 2026

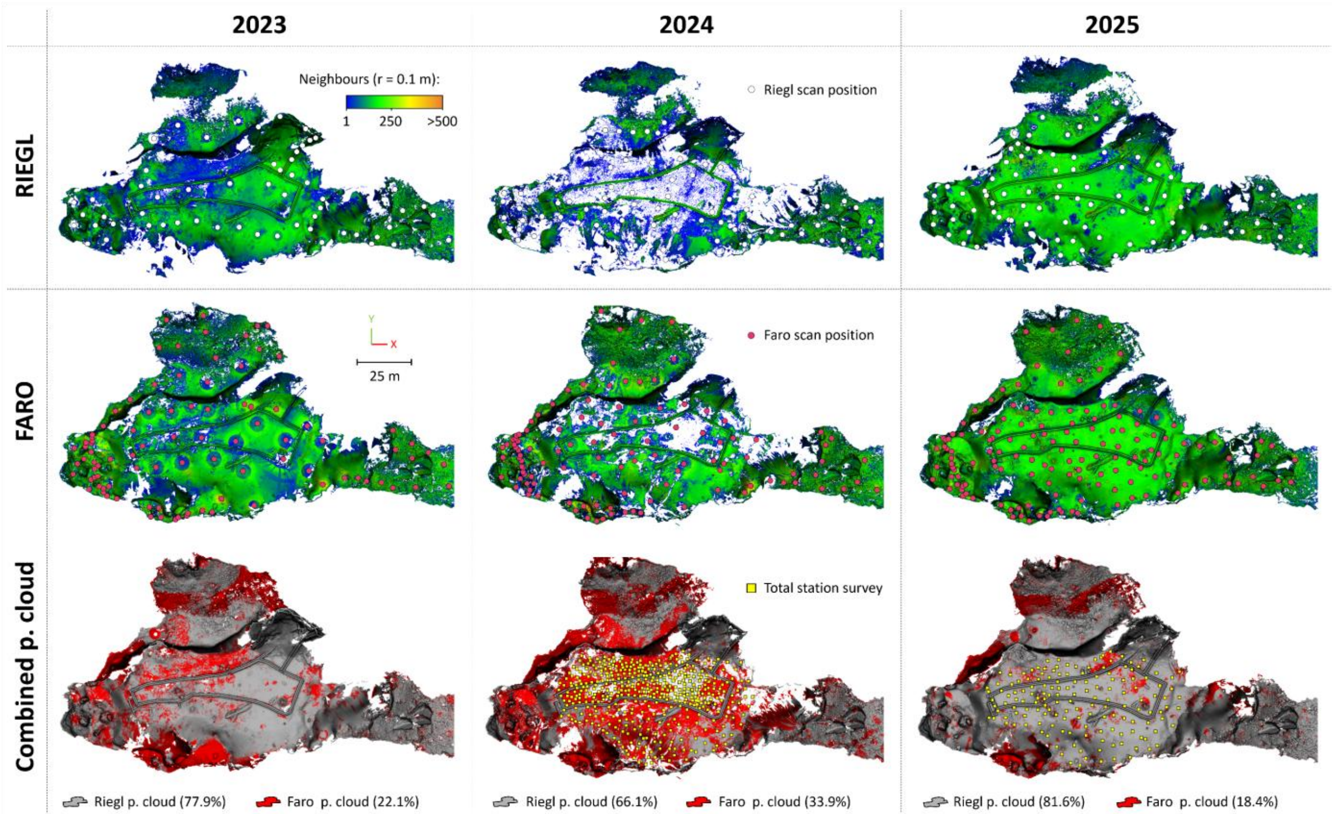

Figure 5: Point cloud coverage of the cave floor around the ice block for individual laser scanners and mapping years, including the distribution of RIEGL and FARO data within the resulting combined point cloud used for DoD processing.

4.2 TLS data quality and surface noise

Several sources of measurement inaccuracy were identified during TLS data-processing (Fig. 6). Positional shifts caused by scanner instability were rare but required exclusion of affected scans (Fig. 6a). Placing the scan position too close to the ice in narrow passages led to higher positional uncertainty, manifested as noise around the ice surface, particularly at low incidence angles (Fig. 6b). Such points were removed by distance filtering and replaced by points from neighbouring positions in overlapping areas. A mirroring effect on melted or transparent ice (Fig. 6c) occurred when the laser pulse was reflected from the ice surface onto a nearby object, causing the return signal to be erroneously positioned as a mirror point beneath the ice surface. These mirrored points had to be removed manually on a scan-by-scan basis because, although they generally exhibited lower backscattered laser intensity than the objects from which they reflected, their intensity values could overlap with those of ice, which needed to be preserved in the point cloud. In addition, close-range low-intensity noise was observed primarily in datasets acquired with the FARO scanner, occurring near the centre of laser scanner positions (Fig. 6d).

https://doi.org/10.5194/egusphere-2026-3512
Preprint. Discussion started: 17 July 2026

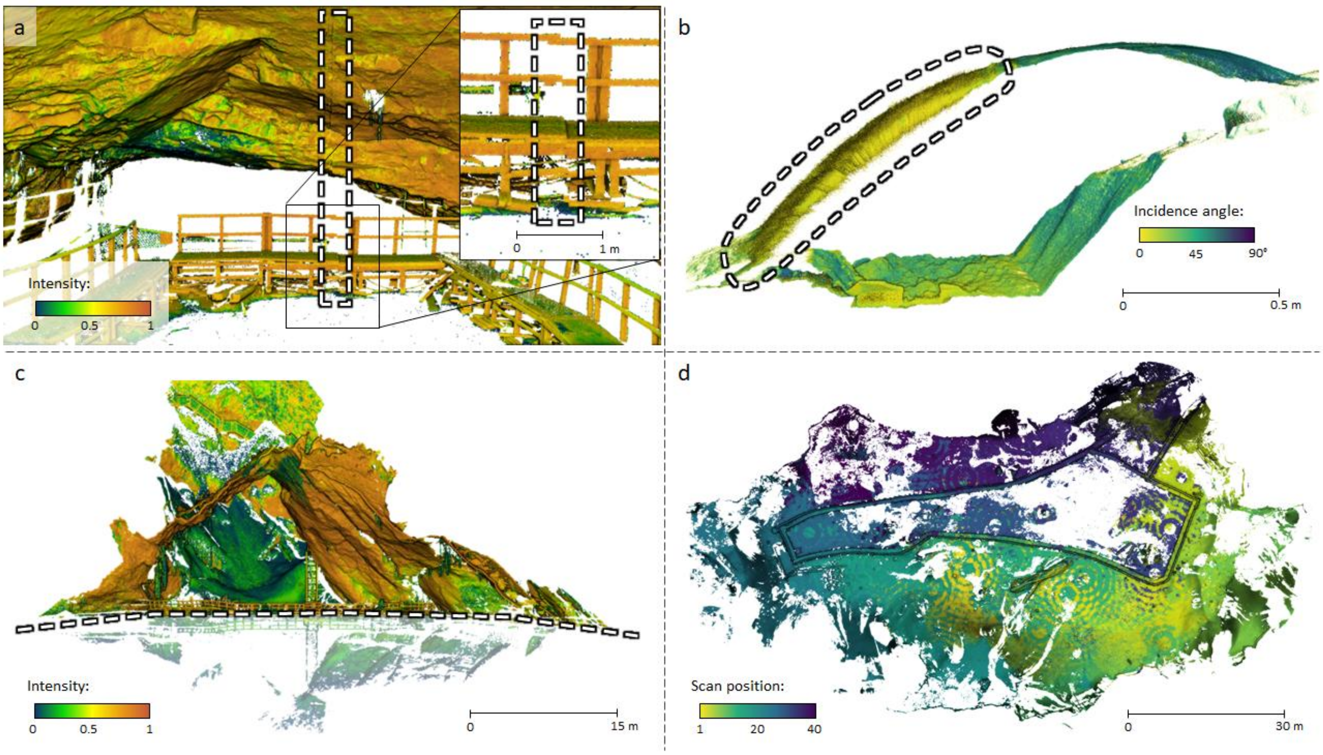

Figure 6: Positional inaccuracies within the collected datasets: a) scan affected by positional shift in the point cloud; b) low incidence angle noise on the ice surface; c) mirroring artefacts caused by false reflections beneath the ice surface; d) radial close-range noise on ice around the centre of FARO scanner positions.

A comparison of FARO and RIEGL point clouds and the processed combined dataset with TSS measurements and derived mesh models across different ice and snow surface types (Fig. 7a–h) reveals systematic differences in noise behaviour, strongly dependent on both scanning range and surface properties. The phase-shift FARO scanner exhibits pronounced range-dependent noise within ~5 m of the scanner (Fig. 6d), reflecting its higher sensitivity to weak and diffuse backscatter at 1550 nm. While the FARO system positional accuracy is reduced on low reflective surfaces such as wet ice and snow, it produces higher point density and homogeneous data coverage. In contrast, the pulse-based RIEGL scanner provides more stable and geometrically accurate measurements with overall lower noise levels. Dust-covered areas (Fig. 7c) and dry, well reflective floor ice and vertical icefalls (Fig. 7a, d) exhibit the lowest noise levels, while inclined and vertical surfaces affected by meltwater or partial transparency, such as icefalls (Fig. 7e, f), ice speleothems (Fig. 7g) and the snow-covered entrance shaft (Fig. 7h), show increased variability and the occurrence of double surface artefacts.

https://doi.org/10.5194/egusphere-2026-3512
Preprint. Discussion started: 17 July 2026

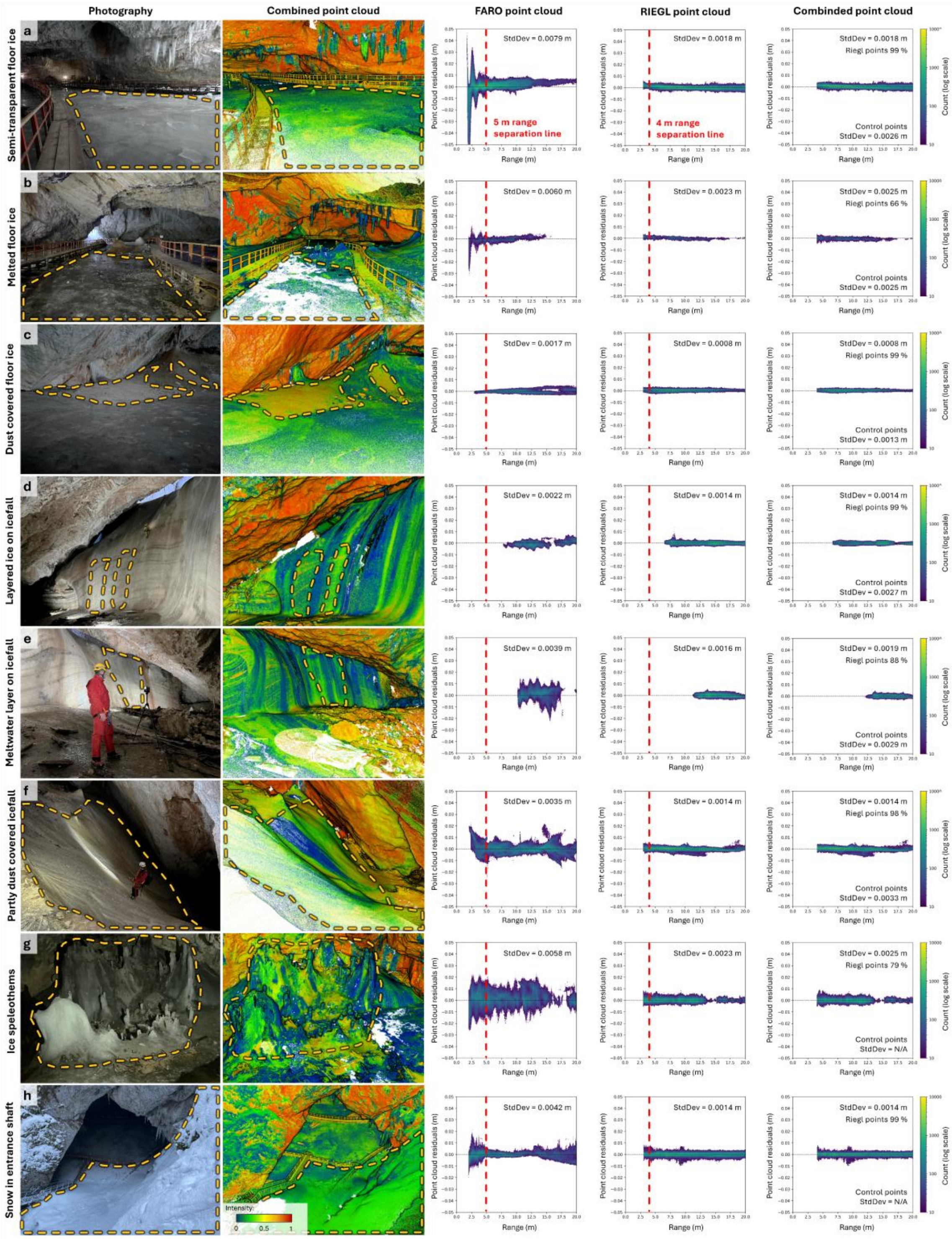

350 **Figure 7: Range-dependent deviation from the reference 3D surface for FARO, RIEGL, and combined point clouds across homogeneous test areas representing different surface types (a–h).**

https://doi.org/10.5194/egusphere-2026-3512
Preprint. Discussion started: 17 July 2026

To further quantify these noise patterns, point-to-mesh residuals were computed as a function of scanning range, intensity and incidence angle against a reference 3D mesh surface for two representative areas (Fig. 8) reflecting the contrasting surface conditions identified in Fig. 7: horizontal semi-transparent floor ice in the Great Hall and a vertical icefall in the Little Reservation. On horizontal floor ice, the raw FARO dataset (9.97 million points, StDev = 13.7 mm) exhibited wide dispersion dominated by close-range noise below ~5 m (Fig. 8a), where residuals reached several centimetres. Beyond this distance, dispersion decreased substantially, indicating that range filtering alone is effective for predominantly horizontal surfaces, consistent with the lower noise levels observed on dry floor ice in Fig. 7a and Fig. 7c. The incidence angle plot confirms that the largest residuals on horizontal ice are concentrated at low incidence angles corresponding to near scanner measurements (Fig. 6d). The raw RIEGL dataset (3.22 million points, StDev = 1.5 mm) showed a significantly lower dispersion with residuals uniformly distributed within the declared scanner accuracy across all ranges (Fig. 8a), intensities and incidence angles, requiring no additional intensity filtering. Range filtering beyond 4 m was applied, as a subtle increase in noise was detected at close-range across several scan positions even above the declared minimum distance of 2.5 m, attributable to the physical properties of the ice surface. On the vertical icefall in Little Reservation (Fig. 8b), the FARO dataset (StDev = 7.8 mm, 99 % range: −17.3 to +17.9 mm) exhibited residuals of approximately ±2 cm distributed across the full range of scanning distances, not concentrated at close-range as on horizontal ice. This behaviour is consistent with the elevated variability observed on meltwater-affected icefalls (Fig. 7e, f) and ice speleothems (Fig. 7g) and indicates that range filtering alone is insufficient for vertical and geometrically complex surfaces, where low reflectivity targets at various distances produce unreliable measurements. The intensity plot (Fig. 8b) reveals that the largest positional errors are associated with low intensity returns regardless of scanning distance, and applying an additional intensity threshold effectively removes these high uncertainty measurements. Unlike on horizontal ice, the incidence angle plot for the icefall shows dispersion distributed uniformly across the full range with an increasing tendency at high incidence angles, visible for both scanners. This is attributable to the wider laser beam footprint capturing objects that do not represent the actual ice surface or splitting on emerging features and surface irregularities when hitting the scanned surface at high incidence angles. The RIEGL dataset on the icefall (StDev = 5.9 mm, 99 % range: −4.6 to +8.5 mm) maintained lower residual bounds but exhibited the same trend, confirming that high incidence angle degradation is geometry driven rather than instrument-specific. The combined filtered point clouds (Fig. 8, bottom rows) reflect the processing workflow described in Sect. 3.3, including noise filtering, scanner-specific range and intensity thresholds, and retention of only those FARO points located more than 2 cm from the corresponding RIEGL surface. On horizontal floor ice, the combined dataset (3.71 million points, StDev = 1.1 mm, 99 % range: −3.3 to +3.1 mm) achieved a twelve-fold reduction in standard deviation relative to the raw FARO data. On the vertical icefall, the combined dataset (6.12 million points, StDev = 2.5 mm, 99 % range: −4.6 to +7.6 mm) shows a three-fold reduction relative to raw FARO and a more than two-fold improvement over raw RIEGL data. Based on the identified noise patterns (Fig. 7, Fig. 8), the range thresholds were set at 4–30 m for RIEGL and 5–20 m with intensity above 0.4 for FARO. A reduced range threshold of 1 m was applied locally in the narrow passage beneath the ice block. The resulting combined point cloud consisted predominantly of RIEGL data (typically 66–99 %), with FARO

https://doi.org/10.5194/egusphere-2026-3512
Preprint. Discussion started: 17 July 2026

providing complementary coverage in meltwater-affected areas. Incidence angle filtering was also considered but does not provide a practical alternative: on horizontal surfaces, low incidence angle noise coincides spatially with the close range zone already removed by range filtering, while on vertical surfaces, where the most problematic measurements occur across all incidence angles at low return intensities, incidence angle filtering would not address the primary source of error that is effectively resolved by intensity filtering.

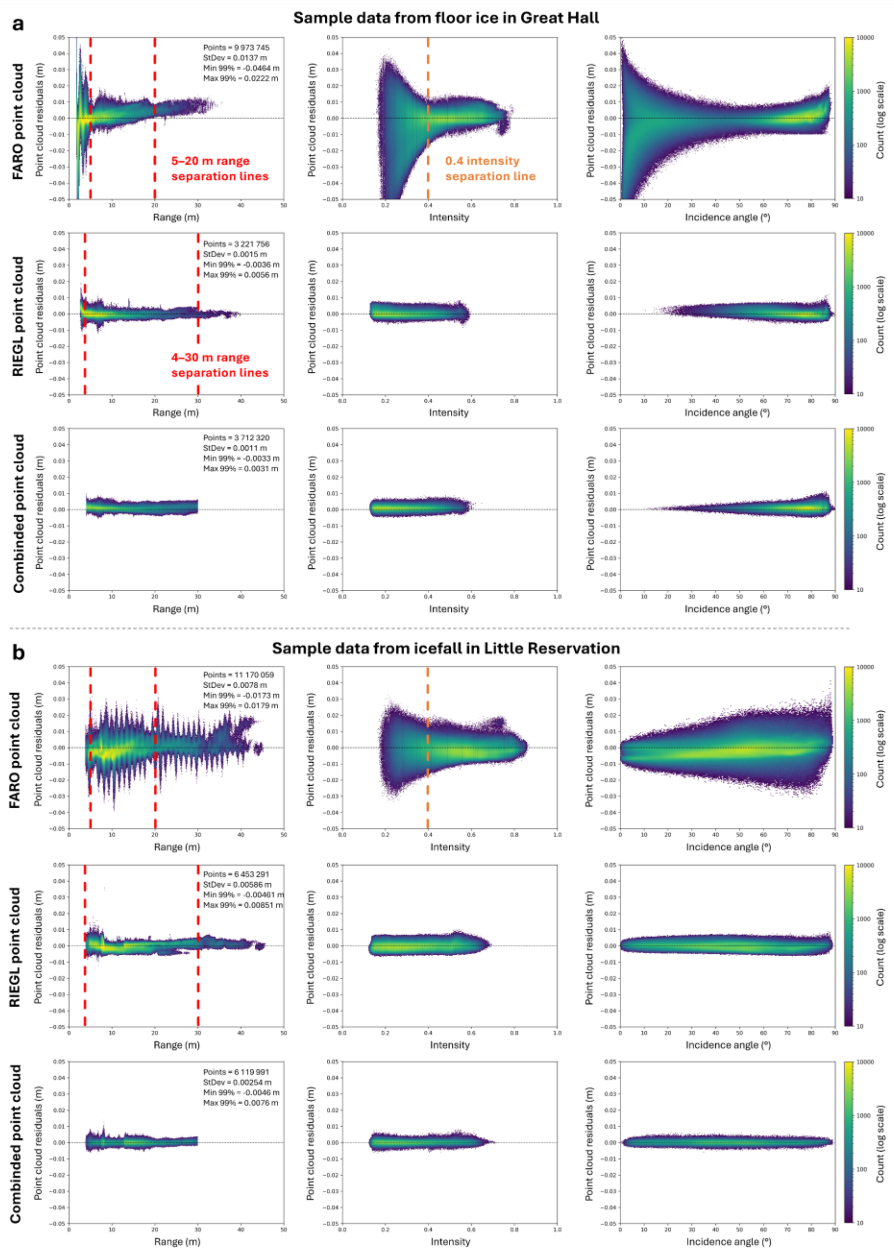

Figure 8: Point cloud residuals against a reference surface as a function of range, intensity and incidence angle represented by sample data a) on floor ice in the Great Hall and b) a vertical icefall in the Little Reservation.

https://doi.org/10.5194/egusphere-2026-3512
Preprint. Discussion started: 17 July 2026

4.3 Evaluation of 3D models and volumetric change

3D models computed at spatial resolutions ranging from 1 to 50 cm were evaluated using reference TSS control points by standard deviation of modelling (E_{Model}) from the 2024 and 2025 surveys (Fig. 9; Table 2). The results indicate an increasing deviation from the control points as the spatial resolution decreases beyond 5 cm. For 2025, the standard deviation increased from ~4 mm at 1–5 cm resolution to about 20 mm at 0.5 m resolution for both Poisson and MeshFix outputs. By contrast, for 2024, applying MeshFix to repair 3D models significantly improved the surface representation, reducing the modelling error from ~55 mm to ~11 mm at finer resolutions and thereby enabling evaluation of data within the AoI with acceptable error even in areas without direct TLS measurements. Consequently, the total error (E_{Total}) and volumetric computation error (E_v) reached their highest values for Poisson results at finer resolutions, ranging from 6.94 to 60.16 mm for E_{Total} and from ±63 to ±600 m^3 for E_V depending on year, method, resolution and surface area (Table 2). Application of MeshFix reduced both E_{Total} and for E_V by up to five times at finer resolution and approximately two times at coarser resolutions.

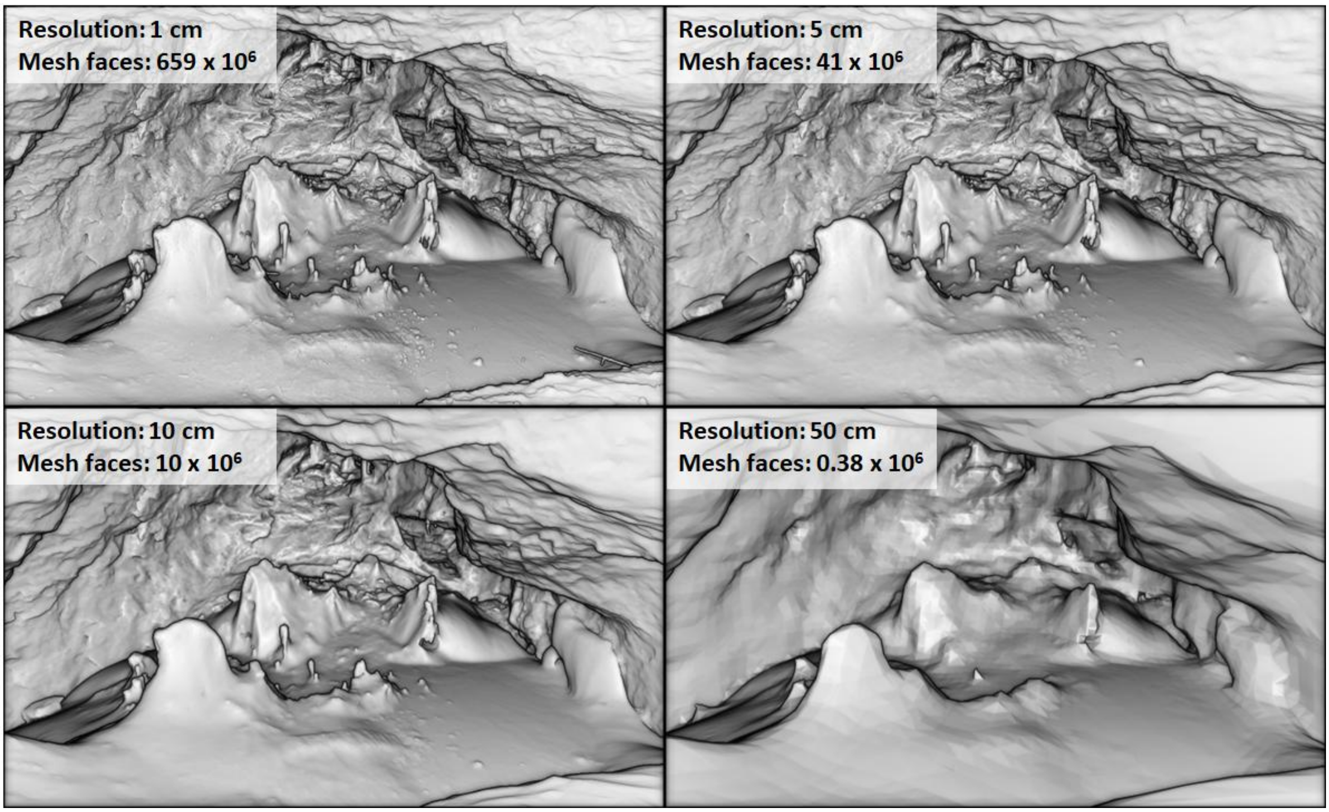

Figure 9: Level-of-detail reduction and surface flattening caused by changes of 3D modelling resolution, demonstrated on floor ice and ice stalagmites in the Church.

Decreasing the modelling resolution reduced the AoI surface (Fig. 9 and Table 2) through flattening and a border effect, in which the AoI polygon clipped small portions of boundary faces and subtle details such as the shapes of stalagmites, narrow ice fissures, or objects trapped in ice (e.g., wood fragments or boulders) leading to potential underestimation of volume

https://doi.org/10.5194/egusphere-2026-3512
Preprint. Discussion started: 17 July 2026

changes in lower resolution. At the same time, reducing spatial resolution decreases the number of mesh faces in the resulting 3D model (Table 2), improving computational efficiency and reducing hardware demands, with model size decreasing from 8.5 GB at 1 cm resolution to 1 GB at 5 cm and 0.01 GB at 50 cm, thereby accelerating subsequent processing and analysis. Given the small differences in total error and mean change within the AoI at 5 cm resolution compared to 2.5 and 1 cm (Table 2), while performing higher smoothing of residual noise and adequate representation of the evaluated ice surfaces (Fig. 9), and significantly reducing computational demands, a 5 cm resolution was selected for further interannual comparison in the established ice accumulations monitoring.

Across the entire AoI, using 2.5D and 3D volume change approaches revealed ~20 % differences in the computed volumes, with the largest differences on the near-vertical ice wall in the Little Reservation, on ice stalagmites and in overhang areas. This is also reflected by the difference in evaluated area from ~9100 m^2 in 3D and ~7200 m^2 in 2.5D, highlighting the necessity of full 3D evaluation at the monitored site. Simple Cloud-to-Cloud approach provided a rough approximation and, where only ice decrease or increase occurred, delivered reasonable mean change estimates that could be converted to volume change using the known AoI area (Fig. 10). The M3C2 approach produced better directionally consistent differences on point clouds and, in the case of uniformly sampled input point cloud with few data gaps, is the most precise method without introducing modelling artefacts (Fig. 10).

3D modelling was required to interpolate data gaps and to compute relevant DoD across the entire AoI for all years because of not uniform point cloud coverage within the AoI (Fig. 5), which reached 85 % and 93 % in 2023 and 2025, respectively, but only 70 % in 2024 as a result of mapping conditions. Using Poisson surface reconstruction alone clearly revealed its drawbacks in 2024 in the flat areas of the Great Hall, on the inclined surfaces between the Church and Rimaye and on the icefall toward the Great Reservation, where multiple modelling artefacts produced unrealistic surfaces with exaggerated increases and decreases when compared with the 2023 and 2025 mapping (Fig. 10). These artefacts were mitigated by MeshFix with reliable results of DoD computation. The use of 3D models was also beneficial in increasing the evaluated area, which was reflected in the average change underestimated by cloud-based approaches due to the data gaps. Taking these factors into account, the most reliable differences were obtained using M3C2 for the point clouds and MeshFix for the 3D models.

The repaired MeshFix 3D models showed an average decrease, relative to 2023, of 3.3 cm in 2024 and 16.6 cm in 2025, with corresponding volume changes of ~ -300 m^3 and ~ -1500 m^3, respectively (Fig. 10). To evaluate the robustness of the detected change, volumetric loss was compared with total propagated uncertainty (Table 2). For 2025, the observed loss of -1500 m^3 substantially exceeds the conservative upper bound of volumetric uncertainty (±186 m^3 at 0.5 m resolution), indicating that the detected change is well above the estimated uncertainty. In contrast, the 2024 loss of -300 m^3 is closer to the uncertainty threshold but remains distinguishable under the selected 5 cm MeshFix configuration (±117 m^3). Under the adopted 5 cm resolution, the minimum detectable volumetric change corresponds to approximately ±117 m^3 (2024) and ±67 m^3 (2025), indicating that only changes exceeding this threshold can be interpreted as physically meaningful.

https://doi.org/10.5194/egusphere-2026-3512
Preprint. Discussion started: 17 July 2026

Table 2: Evaluation of 3D modelling.

Res. (cm)	Method	Year	Mesh Faces	Area (m²)	ΔV (m³)	Δh (cm)	E_{Model} (mm)	E_{Total} (mm)	E_V (m³)
1	Poisson	2023	633 781 777	9396	-1517.95	-16.2	N/A	7.15	67.22
1	Poisson	2024	652 925 497	10 303	-1080.72	-9.5	56.43	56.71	584.20
1	Poisson	2025	632 236 831	9721	Ref.	Ref.	4.45	7.11	69.11
1	MeshFix	2023	658 871 196	9370	-1526.05	-16.3	N/A	7.15	67.04
1	MeshFix	2024	623 716 488	9450	-1203.53	-12.7	11.30	12.58	118.90
1	MeshFix	2025	648 546 879	9662	Ref.	Ref.	4.45	7.11	68.69
2.5	Poisson	2023	151 161 801	9361	-1502.71	-16.1	N/A	7.11	66.57
2.5	Poisson	2024	138 311 941	9624	-1005.08	-10.4	59.91	60.16	579.02
2.5	Poisson	2025	154 803 133	9658	Ref.	Ref.	4.38	7.07	68.24
2.5	MeshFix	2023	152 002 144	9334	-1516.23	-16.2	N/A	7.11	66.38
2.5	MeshFix	2024	141 823 526	9415	-1223.95	-13.0	11.54	12.80	121.77
2.5	MeshFix	2025	156 208 203	9688	Ref.	Ref.	4.38	7.07	68.45
5	Poisson	2023	40 504 520	9142	-1515.42	-16.6	N/A	6.98	63.84
5	Poisson	2024	36 518 136	9384	-908.20	-9.8	55.29	55.56	521.42
5	Poisson	2025	40 398 330	9402	Ref.	Ref.	4.17	6.94	65.23
5	MeshFix	2023	41 622 026	9071	-1521.58	-16.6	N/A	6.98	63.35
5	MeshFix	2024	37 604 492	9254	-1208.68	-13.1	11.37	12.64	117.02
5	MeshFix	2025	41 131 846	9395	Ref.	Ref.	4.17	6.94	65.17
10	Poisson	2023	10 211 884	8602	-1559.76	-17.1	N/A	7.75	66.64
10	Poisson	2024	9 274 042	8754	-1067.00	-11.7	41.51	41.88	366.61
10	Poisson	2025	10 047 664	9196	Ref.	Ref.	5.35	7.70	70.85
10	MeshFix	2023	10 444 144	8576	-1586.42	-17.4	N/A	7.75	66.43
10	MeshFix	2024	9 541 516	8683	-1133.54	-12.4	17.88	18.72	162.52
10	MeshFix	2025	10 194 772	9170	Ref.	Ref.	5.35	7.70	70.65
25	Poisson	2023	1 587 864	8457	-1553.06	-17.6	N/A	15.80	133.59
25	Poisson	2024	1 472 984	8640	-1111.05	-12.6	33.34	33.80	292.33
25	Poisson	2025	1 552 730	9017	Ref.	Ref.	14.77	15.78	142.26
25	MeshFix	2023	1 623 384	8444	-1551.64	-17.6	N/A	15.80	133.36
25	MeshFix	2024	1 502 360	8610	-1156.00	-13.2	16.25	17.17	147.80
25	MeshFix	2025	1 578 304	8972	Ref.	Ref.	14.77	15.78	141.54
50	Poisson	2023	383 190	8462	-1530.34	-18.1	N/A	20.64	174.61
50	Poisson	2024	361 242	8583	-1087.54	-12.8	42.05	42.42	364.11
50	Poisson	2025	373 580	9033	Ref.	Ref.	19.86	20.62	186.26
50	MeshFix	2023	385 298	8451	-1535.41	-18.2	N/A	20.64	174.40
50	MeshFix	2024	365 876	8529	-1111.63	-13.2	34.65	35.09	299.28
50	MeshFix	2025	376 172	9012	Ref.	Ref.	19.86	20.62	185.83

https://doi.org/10.5194/egusphere-2026-3512
Preprint. Discussion started: 17 July 2026

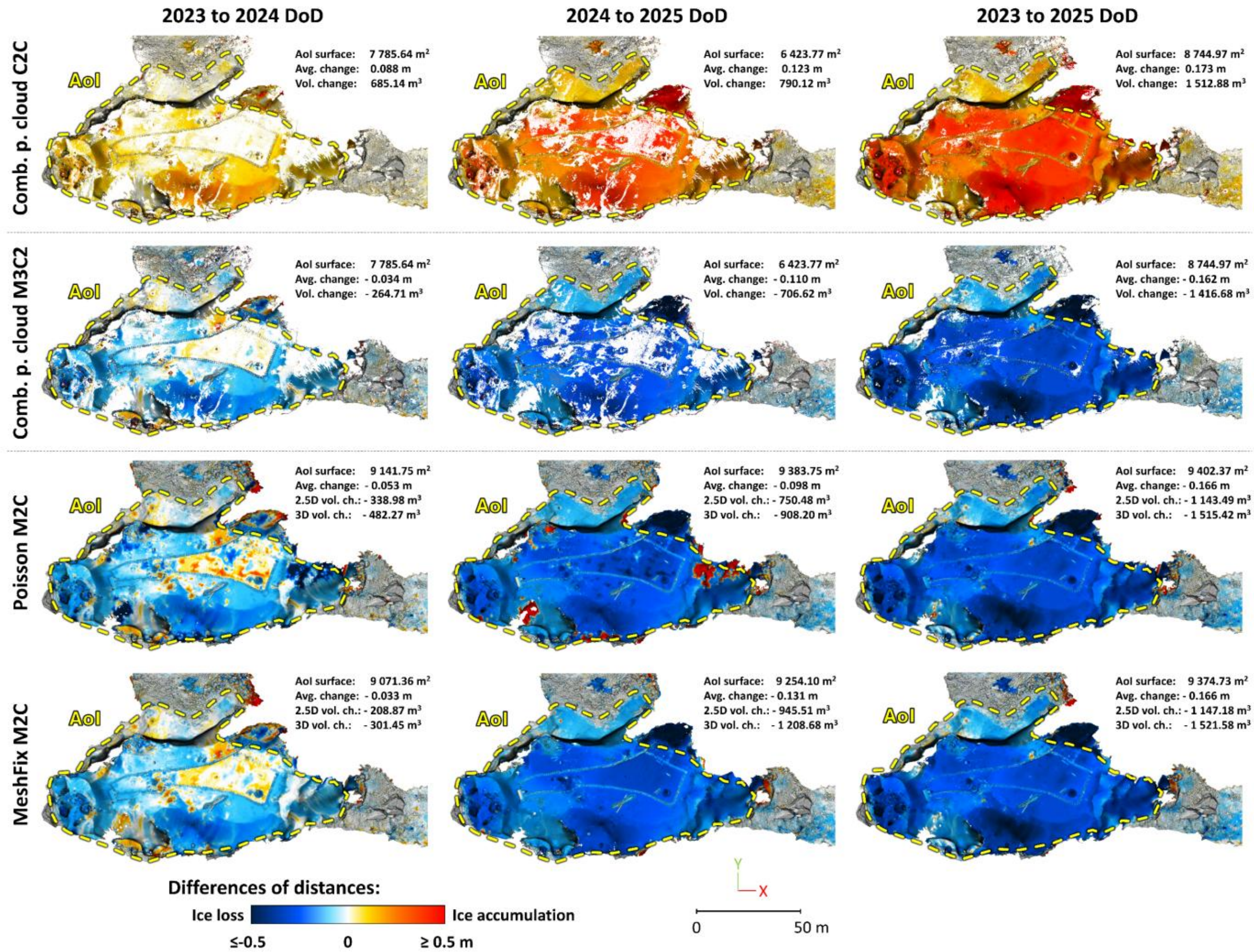

Figure 10: Differences of distances between campaigns, compared using point cloud and 3D mesh model approaches.

Spatial analysis of the MeshFix M2C DoD results revealed substantial heterogeneity in melt patterns (Fig. 10 and Fig. 11). In 2024 relative to 2023, the 95th percentile of negative change was −14.8 cm. Surface change ranged from −74 cm to +64.3 cm; 34.1 % of the AoI experienced a lowering greater than 5 cm, 11.5 % exceeded 10 cm, and 17.6 % remained within ±1 cm. In 2025, relative to 2023, the 95th percentile of surface lowering decreased to −38.27 cm. Surface change ranged from −348.6 cm to +59.7 cm; 81.9% of the AoI experienced a lowering greater than 5 cm, 65 % exceeded 10 cm, and only 5.6 % remained within ±1 cm. When comparing 2025 to 2024, the 95th percentile of negative change was −28.4 cm. Surface change ranged from −340.4 cm to +51.1 cm; 76.2 % of the AoI experienced a lowering greater than 5 cm, 51.2 % exceeded 10 cm, and only 6.9 % remained within ±1 cm. The spatial standard deviation of DoD values increased from 3.8 cm in 2024 to 9.5 cm in 2025, indicating greater spatial heterogeneity of measured surface change. The wide range of difference values

https://doi.org/10.5194/egusphere-2026-3512
Preprint. Discussion started: 17 July 2026

results from the evolution of localized vertical features, namely the complete melting of ice stalagmites and the growth of new ones mainly in the Church, which produce changes far exceeding the average floor-level melt.

The volume change calculated from the difference between the volumes of enclosed manifold 3D mesh models in 5 cm with an identical basal surface is -317 m³ between 2023 and 2024, -1213 m³ between 2024 and 2025, and -1530 m³ between 2023 and 2025. After accounting for possible differences in how the basal surface was closed towards the ice surface and in the distance calculation, these values are in close agreement with the 3D volume changes obtained using the MeshFix and M2C method (Fig. 10), with a maximum difference of 15 m³.

At the local scale, the DoD results reveal spatially heterogeneous patterns of cave ice change, reflecting both accumulation and ablation processes across the cave. In 2024, the largest floor-ice increases within the AoI occurred in parts of the Great Hall, Rimaye and Little Reservation (Fig. 11a1–a3), where numerous new ice stalagmites had formed over the preceding winter. During the 2025 mapping, new ice accumulations were not frequent due to dry winter conditions, with only a few cases in the dripping zone between the Church and Rimaye and a small number of ice stalagmites in the Great Hall and Little Reservation, some of which were even larger than in 2023 (Fig. 11b1–b3). Elsewhere, continued melting of cave ice was observed, with the highest retreat on ice stalagmites in the Church (Fig. 11b3) and on the uppermost inclined parts of perennial ice block in the Great Hall (Fig. 11b1) with areas of considerable inflow of drip-water during the year. These patterns likely reflected a lack of water necessary to form new ice formations and the recycling of melted and refrozen water on lower flat areas, where smaller differences were observed (Fig. 10). Within the Great Reservation, small areas of new ice accumulations were observed, related to the drip-water inflow, while the remaining areas continued to melt in 2024 and 2025 respectively (Fig. 11 a4 and b4). Areas outside the AoI in the Little Reservation showed small patches of melting seasonal ice stalagmites and in the Great Reservation exhibited decreases consistent also with observable buried ice loss (Fig. 10). Visible debris movement in the Great Reservation resulted in apparent increases in the lower parts, reflecting downslope redistribution of material (Fig. 10). Because of the thick snow cover present in 2023 and 2024 and the snow-free conditions in 2025, the entrance shaft was excluded from interannual comparison to avoid misinterpretation of snow-related volume changes.

https://doi.org/10.5194/egusphere-2026-3512
Preprint. Discussion started: 17 July 2026

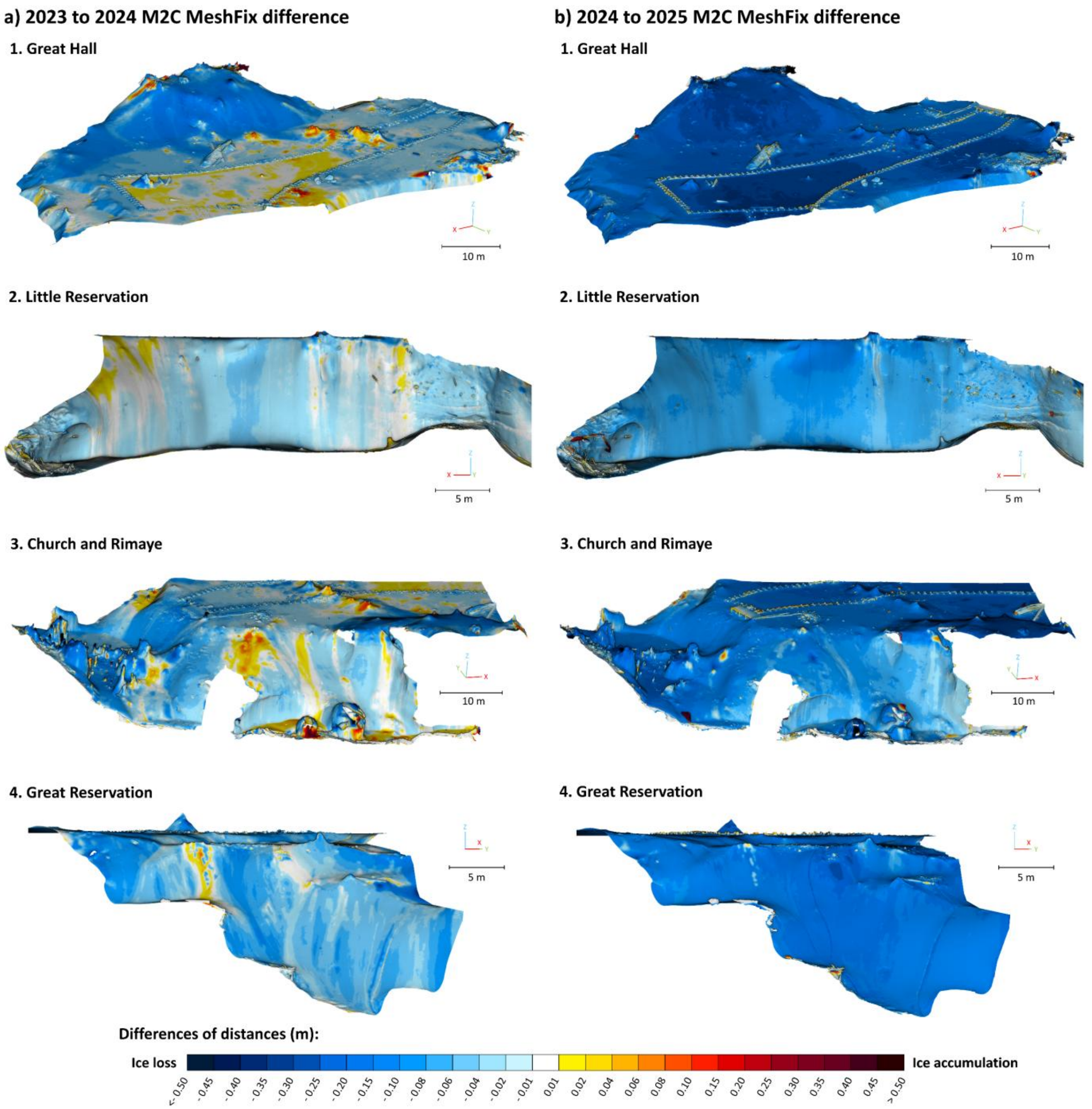

Figure 11: M2C distance differences on ice surfaces between selected periods, using MeshFix 3D mesh models to show different views of representative parts of the cave.

https://doi.org/10.5194/egusphere-2026-3512
Preprint. Discussion started: 17 July 2026

5 Discussion

Reliable volumetric change detection of cave ice requires not only appropriate instrumentation but also a systematic understanding of how acquisition conditions, scanner characteristics and processing steps interact and affect the results. At Scărişoara Ice Cave, systematic noise characterisation across different ice surface types and scanning geometries (Fig. 7, Fig. 8) made it possible to trace specific noise patterns to their physical causes and to define filtering thresholds on a data-driven basis representing a step often applied empirically or not reported in comparable studies. Under favourable conditions for data acquisition, as encountered during the 2023 and 2025 campaigns, a single pulse-based scanner provided sufficient coverage and accuracy for reliable DoD computation. However, widespread meltwater presence in 2024 substantially reduced coverage from the RIEGL scanner alone, and FARO data represented 22–34 % of the combined point cloud in the affected year, compensating for gaps in narrow passages and meltwater affected areas. Multi-source acquisition proved valuable under wet conditions but is not always necessary, and the decision should depend on the surface conditions expected at the time of survey. Regardless of the used device, each data source must undergo an explicit noise assessment procedure and appropriate filtering before integration. The main challenge is therefore not simply scanner choice, but the interaction between wavelength, surface state, scanning geometry and timing of data acquisition.

To overcome the limitation of melt-induced data gaps in TLS datasets, the proposed workflow combines Poisson surface reconstruction and subsequent MeshFix model repair, providing an effective way to obtain a usable surface model for interannual comparison. This hybrid approach significantly improves surface reconstruction and enables reliable volumetric comparison across the full AoI extent. A key strength of the method is the reduction of modelling uncertainty in gap-affected areas, improving the consistency of reconstructed surfaces compared to Poisson models, particularly at higher resolutions. Minimal difference was observed between the Poisson and MeshFix model in 2025 because of high AoI data coverage (93 %) and nearly all reference points lay in areas without significant data gaps, thus the filling procedure was not applied to the evaluated areas. For the 2024 dataset affected by extensive data gaps, coarser Poisson modelling resolutions produced results closer to the actual ice surface and were therefore more suitable for rough estimates with 2–3 times higher volumetric errors, whereas high-resolution models generated without gap filling contained numerous modelling artefacts that biased the estimated volume change by up to ~25 %. These findings indicate that the hybrid modelling approach combining Poisson reconstruction with MeshFix gap filling improved surface representation across all tested spatial resolutions, with the strongest benefit observed for the 2024 dataset at finer resolutions. However, the gap filling procedure may introduce artefacts in areas of complex geometry, particularly near objects embedded in the ice, ice speleothems, fissures, and sharp transitions where the point cloud does not adequately cover the ice surface. In such cases, reconstructed surfaces may deform or entirely suppress small structures. The presented method therefore improves areal completeness, but it does not fully replace missing geometric information.

The comparison between 2.5D and full 3D quantification further demonstrates that a full 3D approach is methodologically necessary at the monitored site. The volumetric difference between the two approaches reached about 20 %, with substantial

https://doi.org/10.5194/egusphere-2026-3512
Preprint. Discussion started: 17 July 2026

discrepancies associated with steep, overhanging and morphologically complex surfaces. Because the 2.5D approach reduces the surface to a single elevation value per pixel, it underrepresents areas with complex 3D geometry, leading not only to lower area estimates but also to biased volumetric change calculations. Given that several published cave ice studies have relied on 2.5D approaches (e.g., rasterised digital elevation models differencing), the magnitude of the bias documented here suggests that volume estimates from morphologically complex cave ice sites based on 2.5D approaches should be interpreted with caution. The M3C2 method offers an alternative that avoids modelling entirely by determining change directly from point clouds along the local surface normal, while explicitly incorporating measurement uncertainty. However, M3C2 requires complete and uniform point cloud coverage of the area of interest; where data gaps exist, cloud-based approaches underestimate the evaluated area and consequently the total volume change. The most reliable results were obtained using point clouds with M3C2 where point cloud coverage was sufficient and MeshFix 3D models with M2C approach where gap filling was necessary.

An additional consideration for volumetric change quantification is the definition of the basal surface used to close the ice body for volume computation. In this study, a consistent basal surface was maintained across all three campaigns to ensure that reported volume differences reflect actual ice change rather than artefacts introduced by varying the reference geometry. In principle, the hypothetical basal surface could be replaced by real subsurface data obtained from ground penetrating radar (GPR) measurements (Securo et al., 2022), which would provide a physically meaningful lower boundary of the ice body. However, low accuracy and spatial resolution of GPR profiles compared with TLS point clouds means that the interpolated basal surface would carry its own uncertainties. More importantly, repeating GPR surveys annually and deriving a new basal surface for each campaign would introduce an additional source of variability into the volumetric comparison, potentially masking or amplifying apparent ice changes and reducing the reliability of reported values. For interannual DoD evaluation, it is therefore preferable to use a fixed basal reference surface throughout the monitoring period, ensuring that volumetric differences are attributable solely to changes in the ice surface captured by TLS.

Volumetric changes quantified at Scărișoara Ice Cave are strongly spatially heterogeneous and do not evolve uniformly from year to year. Smaller ice forms, such as seasonal speleothems, showed faster changes, whereas more extensive parts of the ice body retreated to a lesser extent. Areas with steep, rugged or vertically complex geometry, especially those directly affected by ceiling drip or thin water films, underwent more pronounced changes than relatively flat sectors without direct water influence. Local changes in the ice surface are thus primarily controlled by morphology and by the spatially differentiated inflow of drip-water, confirming that the interannual evolution of cave ice is not governed by a single ablation phase but by the interaction of local topography, microclimate and hydrological forcing. The observed development is broadly consistent with cave ice monitoring results from other European sites, where negative mass balance and strong spatial variability have been reported in most cases. In Silická ľadnica, continuous ice volume loss was recorded with a direct relationship to the cave microclimatic regime and the seasonality of ablation and accumulation processes (Šupinský et al., 2019). In Dobšinská Ice Cave, ice volume decreases of up to 667 m^3 were documented in some sections between 2018 and 2023, while a slight increase was observed in other parts of the cave (Pukanská et al., 2024; Dušeková et al., 2024).

https://doi.org/10.5194/egusphere-2026-3512
Preprint. Discussion started: 17 July 2026

Pfeiffer et al. (2023) recorded an average surface lowering of ~0.06 m over five weeks in Hundsalm Ice Cave, with spatially differentiated patterns. Long-term monitoring in the Julian Alps ice caves revealed alternating seasonal gains and losses sensitive to current meteorological conditions (Securo et al., 2022). A notable exception is Eisriesenwelt, where a slight ice volume increase of ~60 m³ was observed due to successful artificial preservation measures (Buchroithner and Gaisecker, 2020). Collectively, these findings indicate that cave ice across Central and Eastern Europe is undergoing net loss in most documented cases, although the overall balance remains spatially differentiated and depends on cave type, morphology, elevation, cave-air circulation, hydrological regime and human impact.

6 Conclusion

The presented study provides a comprehensive TLS data-processing framework for volumetric change detection of cave ice, systematically evaluating the impact of key methodological decisions, including noise filtering, surface reconstruction, modelling resolution, and the choice between 2.5D and full 3D approaches, on the reliability of reported ice volume estimates. A particular focus is placed on adverse acquisition conditions under which conventional approaches are affected by data gaps, noise, and inconsistent surface representation. The results show that these limitations can be effectively mitigated through the proposed processing chain covering all key steps from noise assessment to volumetric change computation. Application at Scărișoara Ice Cave across three annual campaigns (2023–2025) revealed a cumulative ice loss of 1521 ± 65 m³, mean surface lowering of 16.6 cm and strongly heterogeneous spatial patterns governed by cave morphology and drip-water inflow. By demonstrating the sensitivity of ice volume estimates to individual processing decisions, the study provides a transferable benchmark for cave ice monitoring in environments where semi-transparent, wet or morphologically complex surfaces challenge standard TLS data processing approaches and demand robust noise reduction and gap filling strategies. Based on these results, the following key recommendations for reliable DoD evaluation of cave ice are formulated:

(1) Under favourable conditions, a single well-characterised laser scanner is sufficient for ice change monitoring. Data acquisition under suboptimal surface conditions should be supplemented by additional data sources (e.g., a different scanner type or method) to improve spatial coverage.

(2) Scanner-specific noise assessment and data-driven filtering based on range, intensity or another meaningful variable are essential for achieving low internal point cloud dispersion. Without this step, measurements with high positional uncertainty propagate into subsequent modelling and bias volumetric results. When combining multiple devices, each data source should undergo explicit noise assessment before integration.

(3) 3D surface modelling should employ gap-aware reconstruction methods, such as the hybrid Poisson–MeshFix approach presented here, to ensure reliable surface representation across the full area of interest.

(4) Volumetric change must be evaluated in 3D to avoid the systematic bias introduced by 2.5D approximations, which can underestimate both the magnitude of volume change and the affected surface area.

(5) When computing volumes using enclosed 3D objects with a basal surface, a consistent reference basal boundary should be maintained across campaigns; replacing it annually, for instance with new GPR measurements, would introduce additional uncertainties and reduce the reliability of reported ice volume changes.
(6) Rigorous error propagation combining device precision, registration, co-registration and modelling uncertainties is essential, with the reported uncertainty of volumetric change reflecting the overall quality of the results.

Code and data availability

Computed DoD results on 3D mesh models are provided through a web interface that enables interactive visualisation of ice accumulation changes during the monitoring period. Converted Nexus 3D models for both Poisson and MeshFix approaches are available at: https://uge-share.science.upjs.sk/webshared/Scarisoara/DoD_Mesh.html
The 3D models are coloured according to DoD results and include tools for clipping and querying differences between individual years. Parts of the cave outside the area of interest (AoI), or those not scanned in consecutive years, may exhibit higher DoD values in the web interface and were therefore excluded from the total volume-change estimations.

Author contributions

JŠ conceptualized the study, developed the methodology, curated the data, performed the formal analysis and investigation, prepared the visualizations, and wrote the original draft of the manuscript. AP contributed to the conceptualization, investigation, project administration, and manuscript review and editing. MN contributed to the investigation, validation, and manuscript review and editing. MG was responsible for funding acquisition and contributed to manuscript review and editing. JK contributed to the investigation and manuscript review and editing.

Competing interests

The authors declare that they have no competing interests.

Financial support

This research was supported by the Slovak Research and Development Agency under Grant No. APVV-22-0024, by the VEGA project No. 1/0780/24, and by projects PN-III- P4-ID-PCE-2020-2723, funded by UEFISCDI Romania and F33031 “Understanding Hydrological Processes in Glacierized catchments under Changing Climate using Isotope Techniques” funded by the International Atomic Energy Agency.

References

Attene, M.: A lightweight approach to repairing digitized polygon meshes, Vis. Comput., 26, 1393–1406, https://doi.org/10.1007/s00371-010-0416-3, 2010.

Bartoš, K., Pukanská, K., Kseňak, Ľ., Gašinec, J., and Bella, P.: Cross-Polarized SfM Photogrammetry for the Spatial Reconstruction of Challenging Surfaces, the Case Study of Dobšiná Ice Cave (Slovakia), Remote Sens., 15, 4481, https://doi.org/10.3390/rs15184481, 2023.

Berenguer-Sempere, F., Gómez-Lende, M., Seranno, E., and de Sanjosé-Blasco, J. J.: Orthothermographies and 3D modeling as potential tools in ice caves studies: the Peña Castil Ice Cave (Picos de Europa, Northern Spain), Int. J. Speleol., 43, 4, https://doi.org/10.5038/1827-806X.43.1.4, 2014.

Blatnik, M., Obu, J., Košutnik, J., and Gabrovšek, F.: Use of terrestrial LiDAR scanner for monitoring of ice thickness in ice caves, in: EuroKarst 2022, Advances in the Hydrogeology of Karst and Carbonate Reservoirs, Málaga, Spain, 22–25 June 2022, 185–192, https://doi.org/10.1007/978-3-031-16879-6_27, 2022.

Buchroithner, M. F. and Gaisecker, T.: Ice surface changes in Eisriesenwelt (Salzburg, Austria) based on LIDAR measurements between 2017 and 2020, Die Höhle, 71, 62–70, 2020.

Cabello, R.: Three.js [code], available at: https://github.com/mrdoob/three.js, last access: 15 June 2026.

Cignoni, P., Ganovelli, F., Gobbetti, E., Marton, F., Ponchio, F., and Scopigno, R.: Batched multi triangulation, in: Proc. IEEE Symp. on Visualization (InfoVis 2005), Minneapolis, USA, 207–214, https://doi.org/10.1109/VISUAL.2005.1532797, 2005.

Colucci, R. R. and Guglielmin, M.: Climate change and rapid ice melt: Suggestions from abrupt permafrost degradation and ice melting in an alpine ice cave, Prog. Phys. Geogr., 43, 561–573, https://doi.org/10.1177/0309133319846056, 2019.

Deems, J. S., Painter, T. H., and Finnegan, D. C.: Lidar measurement of snow depth: a review, J. Glaciol., 59, 467–479, https://doi.org/10.3189/2013JoG12J154, 2013.

Dušeková, L., Herich, P., Pukanská, K., Bartoš, K., Kseňak, Ľ., Šveda, J., and Fehér, J.: Comparison of non-contact measurement technologies applied on the underground glacier—the choice for long-term monitoring of ice changes in Dobšiná ice cave, Remote Sens., 16, 3870, https://doi.org/10.3390/rs16203870, 2024.

FARO: Focus X130 HDR laser scanner – technical specification sheet [data sheet], available at: https://download.faro.com/ui/core/index.html?mode=public&referrer=%2Furl%2Fvvemg3krbajfqgrw#expl-tabl./SHARED/%2119sFFH85QXxoD/9G7fRLm55woZS5rm, last access: 15 June 2026.

Feurdean, A., Perşoiu, A., Pazdur, A., and Onac, B. P.: Evaluating the palaeoecological potential of pollen recovered from ice in caves: A case study from Scărişoara Ice Cave, Romania, Rev. Palaeobot. Palyno., 165, 1–10, https://doi.org/10.1016/j.revpalbo.2011.01.007, 2011.

Fuhrmann, K.: Monitoring the disappearance of a perennial ice deposit in Merrill Cave, J. Cave Karst Stud., 69, 256–265, 2007.

https://doi.org/10.5194/egusphere-2026-3512
Preprint. Discussion started: 17 July 2026

Gabbud, C., Micheletti, N., and Lane, S. N.: Lidar measurement of surface melt for a temperate Alpine glacier at the seasonal and hourly scales, J. Glaciol., 61, 963–974, https://doi.org/10.3189/2015JoG14J226, 2015.

Gašinec, J., Gašincová, S., Černota, P., and Staňková, H.: Uses of terrestrial laser scanning in monitoring of ground ice within Dobšinská Ice Cave, J. Polish Mineral Eng. Soc., 30, 31–42, 2012.

Girardeau-Montaut, D.: CloudCompare [software], available at: https://www.cloudcompare.org/, last access: 15 June 2026.

Itcus, C., Pascu, M. D., Lavin, P., Perşoiu, A., Iancu, L., and Purcarea, C.: Bacterial and archaeal community structures in perennial cave ice, Sci. Rep., 8, 15671, https://doi.org/10.1038/s41598-018-34106-2, 2018.

IPCC: Summary for Policymakers, in: IPCC Special Report on the Ocean and Cryosphere in a Changing Climate, edited by: Pörtner, H.-O. et al., Cambridge University Press, 2019.

Jouzel, J.: A Brief History of Ice Core Science over the Last 50 yr, Clim. Past, 9, 2525–2547, https://doi.org/10.5194/cp-9-2525-2013, 2013.

Kazhdan, M. and Hoppe, H.: Screened poisson surface reconstruction, ACM Trans. Graph., 32, 1–13, https://doi.org/10.1145/2487228.2487237, 2013.

Kern, Z., Bočić, N., and Sipos, G.: Radiocarbon-dated vegetal remains from the cave ice deposits of Velebit mountain, Croatia, Radiocarbon, 60, 1391–1402, https://doi.org/10.1017/RDC.2018.108, 2018.

Kern, Z., Molnár, M., Svingor, É., Perşoiu, A., and Nagy, B.: High-resolution, well-preserved tritium record in the ice of Bortig Ice Cave, Bihor Mountains, Romania, Holocene, 19, 729–736, https://doi.org/10.1177/095968360910529, 2009.

Kern, Z., Palcsu, L., Pavuza, R., and Molnár, M.: Age estimates on the deposition of the cave ice block in the Saarhalle Dachstein-Mammoth Cave (Mammuthöhle, Austria) based on 3H and 14C, Radiocarbon, 60, 1379–1389, https://doi.org/10.1017/RDC.2018.96, 2018.

Kern, Z. and Perşoiu, A.: Cave ice–the imminent loss of untapped mid-latitude cryospheric palaeoenvironmental archives, Quaternary Sci. Rev., 67, 1–7, https://doi.org/10.1016/j.quascirev.2013.01.008, 2013.

Kern, Z. and Perşoiu, A.: A review of ice core drilling in cave environment – challenges, achievements and future directions, Front. Earth Sci., 9, 720038, https://doi.org/10.3389/feart.2021.720038, 2022.

Lague, D., Brodu, N., and Leroux, J.: Accurate 3D comparison of complex topography with terrestrial laser scanner: Application to the Rangitikei canyon (NZ), ISPRS J. Photogramm., 82, 10–26, https://doi.org/10.1016/j.isprsjprs.2013.04.009, 2013.

Marzeion, B., Jarosch, A. H., and Gregory, J. M.: Feedbacks and mechanisms affecting the global sensitivity of glaciers to climate change, The Cryosphere, 8, 59–71, https://doi.org/10.5194/tc-8-59-2014, 2014.

May, B., Spötl, C., Wagenbach, D., Dublyansky, Y., and Liebl, J.: First investigations of an ice core from Eisriesenwelt cave (Austria), The Cryosphere, 5, 81–93, https://doi.org/10.5194/tc-5-81-2011, 2011.

Milius, J. and Petters, C.: Eisriesenwelt – From laser scanning to photo-realistic 3D model of the biggest ice cave on Earth, in: GI-Forum 2012, Salzburg, Austria, 3–6 July 2012, 513–523, 2012.

https://doi.org/10.5194/egusphere-2026-3512
Preprint. Discussion started: 17 July 2026

Mineo, C., Pierce, S. G., and Summan, R.: Novel algorithms for 3D surface point cloud boundary detection and edge reconstruction, J. Comput. Des. Eng., 6, 81–91, https://doi.org/10.1016/j.jcde.2018.02.001, 2019.

Mondini, A., Donhauser, J., Itcus, C., Marin, C., Perşoiu, A., Lavin, P., and Purcarea, C.: High-throughput sequencing of fungal communities across the perennial ice block of Scărişoara Ice Cave, Ann. Glaciol., 59, 134–146, https://doi.org/10.1017/aog.2019.6, 2018.

Ohata, T., Furukawa, T., and Osada, K.: Glacioclimatological study of perennial ice in the Fuji ice cave, Japan. Part 2: interannual variation and relation to climate, Arct. Alp. Res., 26, 238–244, 1994.

Păun, V. I., Icaza, G., Lavin, P., Marin, C., Tudorache, A., Perşoiu, A., and Purcarea, C.: Total and potentially active bacterial communities entrapped in a late glacial through holocene ice core from Scarisoara Ice Cave, Romania, Front. Microbiol., 10, 1193, https://doi.org/10.3389/fmicb.2019.01193, 2019.

Perşoiu, A., Buzjak, N., Onaca, A., Pennos, C., Sotiriadis, Y., Ionita, M., Zachariadis, S., Kosutnik, J., Hegyi, A., and Butorac, V.: Record summer rains in 2019 led to massive loss of surface and cave ice in SE Europe, The Cryosphere, 15, 2383–2399, https://doi.org/10.5194/tc-15-2383-2021, 2021.

Persoiu, A. and Pazdur, A.: Ice genesis and its long-term mass balance and dynamics in Scarisoara Ice Cave, Romania, The Cryosphere, 5, 45–53, https://doi.org/10.5194/tc-5-45-2011, 2011.

Perşoiu, A. and Lauritzen, S. E. (Eds.): Ice Caves, Elsevier, 752 pp., https://doi.org/10.1016/C2016-0-01961-7, 2018.

Perşoiu, A., Onac, B. P., Wynn, J. G., Bojar, A. V., and Holmgren, K.: Stable isotope behavior during cave ice formation by water freezing in Scărişoara Ice Cave, Romania, J. Geophys. Res.-Atmos., 116, D02111, https://doi.org/10.1029/2010JD014477, 2011.

Perşoiu, A., Onac, B. P., Wynn, J. G., Blaauw, M., Ionita, M., and Hansson, M.: Holocene winter climate variability in Central and Eastern Europe, Sci. Rep., 7, 1–8, https://doi.org/10.1038/s41598-017-01397-w, 2017.

Perşoiu, A. and Onac, B. P.: Ice in caves, in: Encyclopedia of Caves, edited by: White, W. B. and Culver, D. C., Academic Press, 553–558, https://doi.org/10.1016/B978-0-12-814124-3.00066-2, 2019.

Petters, C., Milius, J., and Buchroithner, M. F.: Eisriesenwelt: Terrestrial laser scanning and 3D visualisation of the largest ice cave on Earth, in: Proceedings of the European LiDAR Mapping Forum, Salzburg, Austria, 29–30 November 2011, 1–10, 2011.

Pfeiffer, J., Rutzinger, M., and Spötl, C.: Terrestrial laser scanning for 3D mapping of an alpine ice cave, Photogramm. Rec., 38, 6–21, https://doi.org/10.1111/phor.12437, 2023.

Pflitsch, A., Schörghofer, N., Smith, S. M., and Holmgren, D.: Massive Ice Loss from the Mauna Loa Icecave, Hawaii, Arct. Antarct. Alp. Res., 48, 33–43, https://doi.org/10.1657/AAAR0014-095, 2016.

Pukanská, K., Bartoš, K., Gašinec, J., Pašteka, R., Zahorec, P., Papčo, J., and Kseňak, Ľ.: Methodological approaches to survey complex ice cave environments – the case of Dobšiná (Slovakia), Front. Environ. Sci., 12, 1484169, https://doi.org/10.3389/fenvs.2024.1484169, 2024.

Rachlewicz, G. and Szczucinski, W.: Seasonal, annual and decadal ice mass balance changes in the ice cave Jaskinia Lodowa w Ciemniaku, the Tatra Mountains, Poland, Theor. Appl. Karstol., 17, 11–18, 2004.

Racoviţă, E. G.: Observations sur la glacière naturelle dite "Gheţarul de la Scărişoara", Bull. Soc. Sci. Cluj, III, 75–108, 1927.

RIEGL: VZ-1000 laser scanner datasheet [data sheet], available at: https://www.riegl-japan.co.jp/product/pdf_1/DataSheet_VZ-1000_2015-01-22.pdf, last access: 15 June 2026.

Securo, A., Forte, E., Martinucci, D., Pillon, S., and Colucci, R. R.: Long-term mass-balance monitoring and evolution of ice in caves through structure from motion–multi-view stereo and ground-penetrating radar techniques, Prog. Phys. Geogr., 46, 422–440, https://doi.org/10.1177/03091333211065123, 2022.

Spötl, C., Reimer, P. J., and Luetscher, M.: Long-term mass balance of perennial firn and ice in an Alpine cave (Austria): Constraints from radiocarbon-dated wood fragments, Holocene, 24, 165–175, https://doi.org/10.1177/0959683613515729, 2014.

Stoffel, M., Luetscher, M., Bollschweiler, M., and Schlatter, F.: Evidence of NAO control on subsurface ice accumulation in a 1200 yr old cave-ice sequence, St. Livres ice cave, Switzerland, Quat. Res., 72, 16–26, https://doi.org/10.1016/j.yqres.2009.03.002, 2009.

Šašak, J., Kaňuk, J., Rusnák, M., and Šupinský, J.: Impact of data structure types and spatial resolution on landslide volumetric change measurements, Geod. Cartogr., 50, 179–197, https://doi.org/10.3846/gac.2024.20647, 2024.

Šupinský, J., Kaňuk, J., Hochmuth, Z., and Gallay, M.: Detecting dynamics of cave floor ice with selective cloud-to-cloud approach, The Cryosphere, 13, 2835–2851, https://doi.org/10.5194/tc-13-2835-2019, 2019.

Šupinský, J., Nováková, M., Gallay, M., and Kaňuk, J.: Microclimatic and ice accumulation change monitoring in Silická ľadnica cave, in: Abstract volume of the 10th International Workshop on Ice Caves, Universität Innsbruck, 36–36, 2024.

Zhang, W., Qi, J., Wan, P., Wang, H., Xie, D., Wang, X., and Yan, G.: An easy-to-use airborne LiDAR data filtering method based on cloth simulation, Remote Sens., 8, 501, https://doi.org/10.3390/rs8060501, 2016.

Zlot, R. and Bosse, M.: Three-dimensional mobile mapping of caves, J. Cave Karst Stud., 76, 191–206, https://doi.org/10.4311/2012ex0287, 2014.

Žák, K., Onac, B. P., and Perşoiu, A.: Cryogenic carbonates in cave environments: A review, Quat. Int., 187, 84–96, https://doi.org/10.1016/j.quaint.2007.02.022, 2008.

Žák, K., Orvošová, M., Filippi, M., Vlček, L., Onac, B. P., Perşoiu, A., and Světlík, I.: Cryogenic cave pearls in the periglacial zones of ice caves, J. Sediment. Res., 83, 207–220, https://doi.org/10.2110/jsr.2013.16, 2013.